Development of a micromachined vaporiser for use in inhalation drug therapy.

Bas de Heij
M.Sc. Physical Engineering University of Twente

Dissertation submitted to the Faculty of Science of the
University of Neuchatel, Switzerland

Insitute of Microtechnology
University of Neuchatel
Rue Jaquet Droz 1
CH-2007 Neuchatel

Development of a Micromachined Vaporiser for use in Inhalation Drug Therapy

Ir. S.C.P. de Heij

June 25, 2000

IMPRIMATUR POUR LA THÈSE

Development of a micromachined vaporiser for use in inhalation drug therapy

de M. Sebastiaan de Heij

UNIVERSITÉ DE NEUCHÂTEL

FACULTÉ DES SCIENCES

La Faculté des sciences de l'Université de Neuchâtel sur le rapport des membres du jury,

MM. N. de Rooij (directeur de thèse), D. Twerenbold,
B. van der Schoot (Neuchâtel) et
M.J. Hess (Neuchâtel)

autorise l'impression de la présente thèse.

Neuchâtel, le 11 mai 2000

Le doyen:

J.-P. Derendinger

Abstract

Inhalation drug therapy is becoming increasingly important as a fast acting non-invasive method of administering drugs. The inhaled mist has to pass most of the anatomy of the human lung which acts as a filter. Only a certain size of particles will be able to pass deep enough in the lungs to have therapeutic effect.

Current devices for aerosol administration are pressurised canisters which use a propellant gas to eject the aerosol. The size distribution of the droplets in the aerosol is large and most of the medicine will never be able to reach the deep lung. The ideal size of the particles lies in the 4 to 5 μm range. All particles that will be inhaled should be at least smaller then 6 μm.

To arrive at an aerosol with a sufficiently small size distribution, drop on demand technique was used. New etching technology (Deep Reactive Ion Etching) permitted the production of nozzles that are small enough to generate the proper particle size for inhalation and which have a low enough flow resistance to be used in a battery operated, portable device.

The basic operation parameter of the device are connected with the resonances and modeshapes. When the actuation frequency is that of the resonance of the right modeshape droplet ejection can occur. Three different designs were optimised using finite element method to address each a particular resonance mode. Two of the designs proved successful, and showed some of the most critical characteristics for use in inhalation drug therapy.

The final device not only has superior characteristics in droplet generation compared to traditional devices, it is also an active element which can be integrated into an intelligent system.

Acknowledgements

There is a number of people without whom this thesis would never have existed in its current form and who I would like to thank for their help, their comments, their ideas, their effort and their friendship. First of all my thesis director and my supervisor and the external thesis experts : Prof. N.F. de Rooij, Bart van der Schoot and D. Twerenbold. I also want the acknowledge the good working atmosphere provided by all my colleagues at the IMT. Of no lesser importance the input from Microfilm Engineering SA, especially J. Hess and Hu Bo. The technicians at both the IMT and Microflow who helped my with the fabrication of the devices need special thanks. Then there are still a number of people that my life worth while these last few years. To all of you would like to say thank you.

The work in this project was financially supported by the Swiss Priority Programme for Micro and Nano Technology (MINAST) under project number 1.06.02.

Neuchâtel, February 2000.

Most of the pictures in this thesis are available in colour from the CD-ROM version.

Contents

Chapter 1

Introduction

1.1 Inhalation Drug Therapy

Inhalation drug therapy (IDT) is becoming increasingly important as a fast acting, non-invasive method for drug administration. It acts on the receptor sites in the deep lung, mostly located on the muscle tissue there. Inhalation as treatment method was already known for centuries in the form of steam and vapour inhalation. The last few decades it found wider application in systematic treatment with the invention of the metered dose inhaler (MDI).

The MDI (see fig.'s 1.1 and 1.2) consists of a pressurised canister, a metering valve and a nozzle. The medicine is filled in the metering valve during priming. When actuating the valve, the metering chamber is connected with the nozzle and the medicine is sprayed out. This spray is subsequently inhaled and transported through the lung to arrive at its target site.

Key characteristic is the size of the droplets in the spray or aerosol. The aerosol coming from the MDI has a rather broad distribution of droplet sizes. Especially the bigger droplets represent a large portion of the total ejected volume as can be seen from fig. 1.3. Due to this distribution the efficacy of the treatment is quite low: only 10 to 20% of the aerosol has the potential to arrive in the deep lung. Droplets that are too big will not arrive deep enough in the lung, others that are too small will be exhaled again [1.1]. Medicine that does not arrive at the right

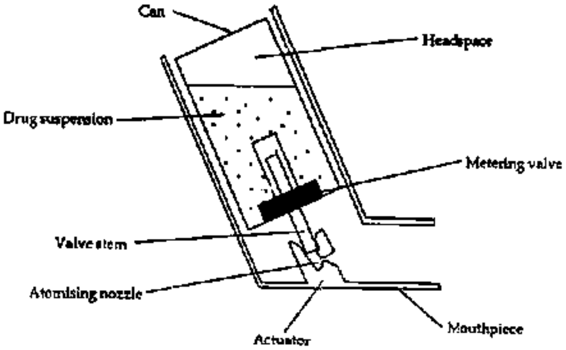

Figure 1.1: *Typical MDI device, it consists of a pressurised canister, metering valve and an atomiser nozzle. The driving force is a propellant gas.*

place is not only lost but can also cause unwanted effects. To produce a finer mist, a propellent gas is used which vaporises during the first phase outside the nozzle and thus shrinking the size of the droplets. One of the goals of this research is to find a method for generating the mist of medicine that does not use a propellant gas and gives a more uniform aerosol.

An other weak point in the MDI's used is that there is no coordination between the generation of the aerosol and the actual inhalation flow. Once activated, the MDI will eject its full dose (see fig. 1.4). Due to poor coordination of the patient, part of the dose can get lost because it never gets properly inhaled.

When an active element is used to vaporise the medicine it will be possible to electronically start and stop the generation of mist. Putting such a device in a system with a micro-controller and a sensor that measures the inhalation flow, will make it possible to use feedback control on the mist generation. Such a device can be called a 'smart inhaler' [1]which would eliminate the coordination problem and will largely improve the effectiveness of the treatment, this in turn improves the quality of life of the patient. It is possible to compute the effective dose that arrived in the deep lung when the airflow is known exactly as well as the aerosol-

---

[1] Trademark of Microflow engineering S.A.

***Figure 1.2**: A collection of inhalers, several MDI devices are shown together with dry powder inhalers which are used in practically the same way as an MDI. (curtesy of the 'Astma Fonds', from the brochure 'Medicijnen', sixth issue 1996.)*

generation-timing. This measurement information can be used as feedback to patient and/or the treating physician. Chapter 2 describes how the optimal droplet size can be found and how to find the total lung dose. Results of this chapter can also be used to find the parameters for the controller.

Currently systems exist that generate an aerosol with a very small size distribution (i.e. a mono-dispersive aerosol) and that are breath actuated. Due to their size and complexity their use is limited to bed side treatment. This project aims to

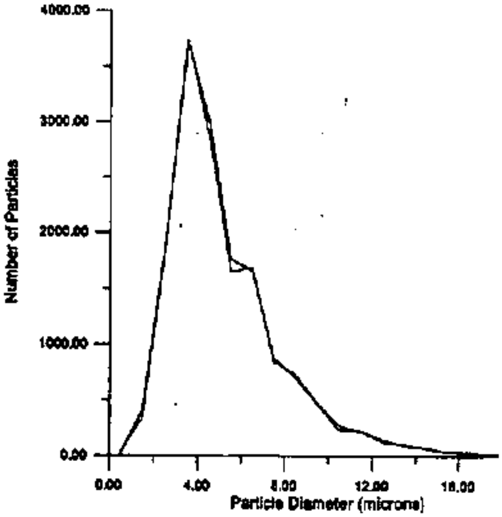

***Figure 1.3**: Size distribution for a traditional MDI as measured by [1.2]*

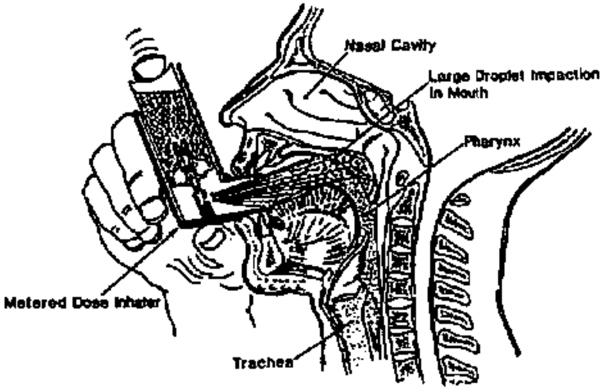

***Figure 1.4**: Normal use of an MDI. The patient has to inhale and at the same time trigger the device.*

develop a portable device so that systematic treatment is possible outside a hospital environment.

1.2 Using Ink-jet techniques

The mist, or aerosol, generated by the MDI has a very broad distribution of sizes (see fig. 1.3). Such an aerosol is called poly-disperse. Only a small part of the distribution, a certain size window, arrives where it is needed. An aerosol with only droplets of one size on the other hand, is called mono-dispersive.

To improve the effectiveness of the treatment the aerosol generator has to be changed to one that is capable of generating such a mono-disperse aerosol. A very common way of generating small droplets of a very precise volume is already used in ink-jet printers but their droplet size is not yet suitable for IDT. The approach for this research is to look at existing ink-jet droplet generators and to use the same basic techniques. Chapter 3 goes into the different techniques reported in literature and will discuss the merits and drawbacks, to arrive at the basic design.

The lowest droplet size reported from an ink-jet type device is in the order of 30 μm diameter, while the demand for IDT lies in the region of 4 to 5 μm diameter. The nozzle size is defining the droplet size, so that smaller as usual ejection nozzles are needed. Disadvantage of such small nozzles is the high flow resistance, which demands high energy for droplet ejection. Shortening the actual channel length of the nozzle, can compensate some of this higher flow resistance.

New Deep Reactive Ion Etching (DRIE [1.3]) techniques make it possible to etch features of only a few microns in size with a maximum ratio between the height and width, the aspect ratio, of 20. This technique can also be used to make very small nozzles in thin membranes, facilitating a low as possible flow resistance.

1.3 Micro-technology

The potential market for an IDT systems is enormous. This means that a vaporiser should be developed that can be mass produced. One of the advantages of using microtechnology is that producing higher numbers is simply done by parallel processing; all similar features are produced at the same time on all devices. This is also called batch processing. Contrary, in traditional technology where every device is processed in a single step fashion.

An other advantage of microtechnology is the accuracy with which devices are produced. There is no wear of tools or something similar so that a constant, high, quality is easily achieved.

1.4 A hand held device

For an IDT device to be useful outside a hospital environment it should be portable and preferably be of such a size that it is easily carried around in e.g. a shirt pocket or handbag. The power consumption of such a device should be so low that reliable operation is possible from a battery. Such a battery should outlast the total number of doses that are ejected from the device.

Most of the time the device will be sitting idle in the shirt pocket or handbag. Depending on the treatment chosen it will be used for one or two times a day, at these times it should function within its specifications (see chapter 2 for details on the demands). The nozzle(s) of the vaporiser should not get clogged due to drying of the medicine. A complicated priming procedure is also not preferable because of the possible excited state of the patient, for instance when an attack is coming. The maximum allowable priming can be activated by opening a protective cover.

1.5 Outline of the thesis

This thesis is a systematic treatment of the research done on the vaporiser element in the 'smart inhaler'. The main goal was to develop a vaporiser that generates a mono-dispersive aerosol which can be electronically controlled. The two main subjects are a computer model of the human lung (chapter 2) and the building of the actual vaporiser (rest of the chapters). The computer model was built to get more insight in the ideal droplet size for inhalation and in the transport mechanisms.

Finally experimental observations on small droplets can be used as feedback to fine tune and perfect the computer model.

The vaporiser was developed, starting from existing droplet generators found in literature (chapter 3). During the first development phase characterisation techniques had to be found and some were partially developed (chapter 4).

After that several series of devices were built by trial and error, and some of the basic operational parameters were understood, a systematic modelling and optimisation procedure was started (chapter 5). This was done to find an improved design that had a better stability and higher efficiency. Finally three optimised designs were fabricated and tested: Chapter 6 shows that we succeeded in developing a vaporiser suitable for inhalation drug therapy.

Bibliography

[1.1] P. Zanen. *Aerosol formulation and clinical efficacy of bronchodilators.* PhD thesis, Universiteit Utrecht, Faculteit geneeskunde, 1999.

[1.2] K.W. Stapleton and W.H. Finlay. Determining solution concentration within aerosol droplets output by jet nebulizers. *J. Aerosol Sci.*, 26(1):137–145, 1995.

[1.3] P.-A. Clerc, L. Dellmann, F. Grétillat, M.-A. Grétillat, P.-F. Indermühle, S. Jeanneret, Ph. Luginbuhl, C. Marxer, T.L. Pfeffer, G.-A. Racine, S. Roth, U. Staufer, C. Stebler, P. Thiébaud, and N.F. de Rooij. Advanced deep reactive ion etching: A versatile tool for micromechanical systems. *Journal of Micromechanics and Microengineering*, 8:272–278, 1998.

Chapter 2

Transport and deposition of particles

Abstract

The different mechanisms involved in the transport and deposition of small particles inside the human lung were investigated. The ideal size of the droplets in the aerosol was calculated using a computer model. To arrive as deep as possible in the lung the droplets should be in the 1 to 2 µm range. The interaction sites for mast medicine are higher up in the lung and to arrive there bigger particles (4 to 5 µm) should be used. The upper limit for particles that can be transported through the lung was found to be 6 µm. Only small differences in the optimal size, were found between the different age groups and different breathing patterns.

2.1 Introduction

The generated aerosol has to enter deep into the lung to have its therapeutic effect. On its way there it passes most of the anatomy of the lung which works as a filter that filters out most of the particles. It is essential to take a closer look at the anatomy and the movement of air in and out of the lung to get a feeling for the filter function and thus the efficiency of the particle transport. The first part of this chapter looks at the anatomy and the air flow in and out of the human lung. If we compare the Reynolds numbers (see table 2.1) of the air flow with the critical value of 1600 we see that mostly a laminar flow can be expected (the first generations of bifurcations might be in the danger zone). This air flow is used as carrier for the aerosol, so particles that follow the streamlines should arrive in the deep lung as the air flow does. There are three mechanisms; sedimentation, diffusion and impaction, that will move the particle away from the streamline and (for a part) towards the lung-wall. Paragraph 2.3 will discuss the different deposition mechanisms and their dependence on flow and geometry.

These factors (airflow and deposition mechanisms) can be combined in a computer programme to arrive at a transport model—and thus the filter function—of the human lung. One computer model specific for finding the optimal particle deposition in the deep lung was constructed. This to gain insight in the different deposition mechanisms and to find out which one causes certain particles to be deposited where. In literature also a number of models can be found, each used for a specific goal. Paragraph 2.4 will discuss these models and the results of our calculations. Finally this information is used to set the droplet size and flow parameters for the aerosol generator.

2.2 The Human Lung

The human lung consists of a series of bifurcating tubes with decreasing diameter and length. E. Weibel [2.1], described these by a regular model where every tube—the parent—splits up into two smaller daughter tubes of equal diameter (see fig. 2.1). Considering the Weibel 'A' model there are 23 generations of airways (i.e. 22 bifurcations) From these the last six are the farthest away from the mouth and hold the alveoli or lung-sacs. It is only there that gas exchange occurs.

Medicine has its therapeutic effect in different area's of the lung depending on the type of medicine [2.2]. Most medicine work in the area of the 17th to 23th generation. All that comes before this area works as a filter with a certain transfer function. Table 2.1 gives the sizes of the tubes as measured by E. Weibel. K. Horsfield *et. al.* [2.3] published a more statistical approach to the lung morphology, where every tube splits up in two unequal branches depending on how the parent tube branched off its parent. To make a computer model of this each individual

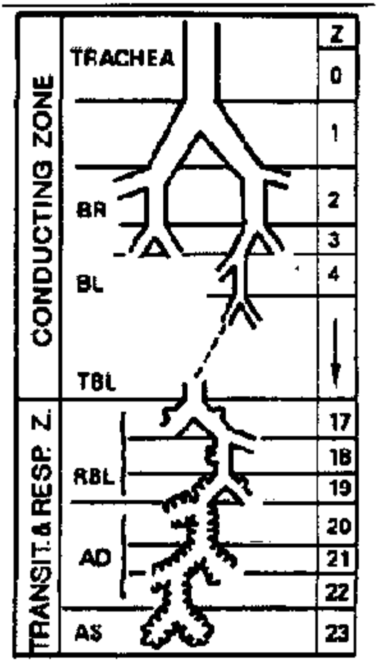

***Figure 2.1**: Schematic view of the human lung, from Weibel [2.1]. The numbers on the right are the generation numbers. Generations 17 and beyond hold the alveoli where the gas exchange takes place. Also in these last generations (17 to 23) the muscle tissue and receptor sites for the most common asthma medicine.*

tube will have to be modelled, contrary to the Weibel model where only one type of tube exists per generation. The Weibel model will be used for the simulations because of its simplicity. Data from Horsfield, on branching angles and radii, will be used to complete the Weibel model. The extra-thoracic part of the airways (i.e. the mouth and throat) are left out of the model as simplification. A properly designed inhaler will show little loss in that area (see also the conclusion and discussion of this chapter)

During inhalation the lung is filled with fresh air. The air is humidified and heated to body temperature in the nasal cavity or—by mouth breathing—in the upper airways. The oxygen in the air is exchanged for CO_2 in the respiratory zone of the lung (see Fig. 2.1. After that the air is exhaled again. The maximum volume of air in the lung is referred to as the Total Lung Capacity (TLC). Under normal breathing conditions the lung is never completely filled to this level. At exhalation

***Table 2.1**: Geometry of the human lung from the Weibel model 'A' [2.1]. Sizes are given for a lung at 75% TLC (see explanation on page 12). The last six generations hold about 3120 cm^3 in alveolar volume in addition to the generation volume. This gives a total volume of 4.2L.*

name	generation number	Width (cm)	length (cm)	volume in generation (cm^3)	Reynolds number
Trachea	0	1.8	12.0	30.52	1965.9
Bronchi	1	1.22	4.76	11.12	1450.2
	2	0.83	1.9	4.11	1065.8
	3	0.56	0.76	1.50	789.9
Bronchioles	4	0.45	1.27	3.31	491.5
	5	0.35	1.07	3.29	315.9
	6	0.28	0.90	3.54	197.5
	7	0.23	0.76	0.17	120.2
	8	0.186	0.64	4.45	74.3
	9	0.154	0.54	5.15	44.9
	10	0.13	0.46	6.25	26.6
	11	0.109	0.39	7.45	15.9
	12	0.095	0.33	9.58	9.1
	13	0.082	0.27	11.67	5.3
	14	0.074	0.23	16.20	2.9
	15	0.066	0.2	22.41	1.6
Terminal and	16	0.06	0.165	30.56	0.9
Respiratory	17	0.054	0.141	42.30	0.5
Bronchioles	18	0.050	0.117	60.19	0.3
	19	0.047	0.099	90.01	0.1
Alveolar-	20	0.045	0.083	138.35	0.1
Ducts	21	0.043	0.070	213.08	0.0
	22	0.041	0.059	326.55	0.0
Alveolar sacs	23	0.041	0.050	553.47	0.0

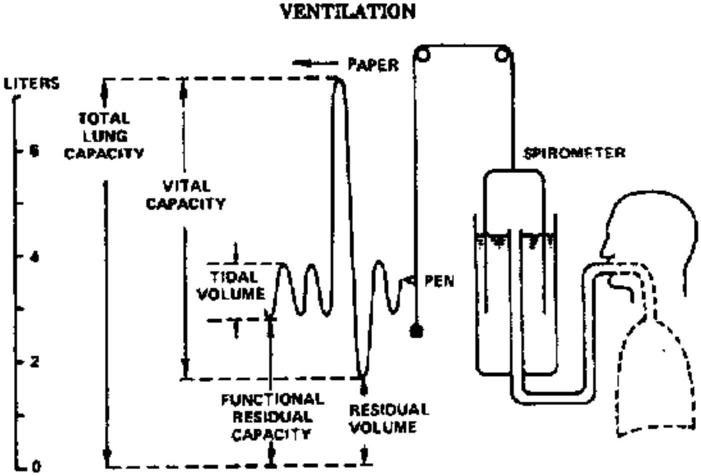

Figure 2.2: *The different characteristics of a breathing cycle [2.4]. The spirometer measures the complement of the total lung capacity.*

the lung is never completely emptied either, a certain volume of air remains; the Functional Residual Capacity (FRC). The volume of inhaled air is called the tidal volume. A comprehensive diagram is shown in fig. 2.2, it shows the lung volume during a breathing cycle. More in-depth information can be found in the book by J. B West [2.4]. Physical exercise will usually give a higher flow, while during sleep it is lower. For an asthmatic these levels and the tidal volume are different from a healthy person. Mostly they are comparable with an healthy person under light exercise conditions [2.5] but with a different lung configuration. Table 2.2 gives a comparison of different breathing patterns characteristic for different groups of people.

The sizes as given by Weibel or Horsfield correspond only to one position or volume of the lung. To arrive at the right sizes during inhalation the diameter and length of the tubes have to be scaled. This makes the lung a very dynamic environment and very hard to model to its full extent, i.e. simplifications have to be applied. Secondly, these models represent a healthy lung, one that needs no medicine. A proper model should account for the obstruction of lung tubes as seen with asthmatics. Kim *et.al.* investigated this and came with 12 characteristic cases. They found that in different subjects different area's (generations) were obstructed. Table 2.3 lists these, where the first column gives the obstructed generation(s) and the second the amount of obstruction. Several of these cases will be investigated with our lung model later on.

***Table 2.2**: Typical breathing patterns [2.6]. The first line of each case is under light exercise and the second under normal breathing conditions.*

	height (cm)	Breathing period (s)	flow (l/min)	Vtidal (ml)	FRC (ml)
male	176	3	50	1250	3300
male	176	4.5	20	750	3300
female	163	2.86	42	992	2681
female	163	2.78	20	464	2681
15y male	169	2.6	46	1000	2677
15y male	169	3.2	20	533	2677
15y female	161	2.5	43	903	2325
15y female	161	2.5	20	417	2325
10y	138	1.875	37	583	1484
10y	138	2	20	333	1484
5y	110	1.3	19	244	767
5y	110	1.28	20	213	767

***Table 2.3**: Different possibilities for obstructions of airways as observed in an asthmatic's lung. The first column lists the obstructed generation(s) and the second the amount of obstruction [2.7].*

obstructed generation(s)	amount of obstruction
3	25 , 40 %
0–3	"
4–7	"
0–7	"
8–16	"
0–16	"

Apart from this there is still the intra and inter patient variability. Which means that the same patient might have a different lung configuration from one inhalation to the next. There are also differences between patients, the inter patient variability. This variation is comparable with the differences in hight and/or weight between the different persons.

The change in air pressure between the mouth and alveoli during breathing is only several mbar. Hence the air flow can be considered incompressible and thus it is sufficient to only look at the mass transport.

Also from table 2.1 can be seen that most of the inhaled volume goes to the last three generations and the alveoli. The first inhaled air will enter the deepest into the lung. The last part of the inhalation will never reach the deep lung. This indicates that it will not be useful to generate an aerosol during all of the inhalation.

2.3 Deposition mechanisms

Small particles are taken inside the lung with the airstream. Without external influence the particles will exactly follow the streamlines of the flow. There are three mechanisms to divert the particles from the streamlines; diffusion, sedimentation and impaction. Each of these will be discussed separately below. It is assumed that the particles will move exactly with the flow if there are no external influences working. The deposition probability can then be calculated from the distance travelled away from the original location on the streamline.

2.3.1 Diffusion

Diffusion is the process that tends to equalise the concentration of a species throughout a continuum. The driving force is the thermal energy, the higher the temperature the faster the diffusion. The general expression for diffusion is Fick's law:

$$\overline{x^2} = 6Dt \tag{2.1}$$

with D the diffusion constant. It expresses the average diffusion distance ($\overline{x}$) after a time t.

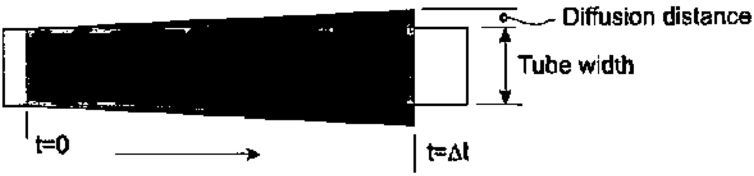

Figure 2.3: *Schematic view of diffusion deposition*

Einstein's expression for diffusion and mobility:

$$D = kT \cdot b \tag{2.2}$$

With b the mobility of the species. To arrive at the mobility we take a look at the friction of a small, round particle with diameter d, moving with a speed v in a fluid of viscosity ν. The friction force equals [2.8]:

$$F_f = 3\pi\nu d v \tag{2.3}$$

From this, one can deduce that the mobility equals:

$$b = \frac{1}{3\pi\nu d} \tag{2.4}$$

Finally this gives the diffusion constant for small particles in a fluid as:

$$D = \frac{kT}{3\pi\nu d} \tag{2.5}$$

If we now look at a particle travelling on a streamline through the lung: after a time Δt it will on average have moved $\sqrt{6\Delta t \cdot D}$ away from its original location on the streamline. It is now possible to construct a sphere with this radius around the original location of the particle. The fraction of the sphere that intersects with the wall is now the deposition probability. A slightly simplified model can be made by looking at this, tube for tube and for all particles at the same time. At the beginning of the tube (at $t = 0$) all particles will be inside the tube. The distribution now moves outwards due to the diffusion (see fig. 2.3). The part of the distribution that falls outside the tube diameter can be considered deposited.

If the particles fall inside a tube with width W at $t = 0$, they will diffuse out to $W + \sqrt{6\Delta t \cdot D}$ after a time Δt (see fig. 2.3). The fraction of particles falling outside the tube is now:

$$C = \frac{(W + \sqrt{6\Delta t \cdot D})^2 - W^2}{W^2} \tag{2.6}$$

This formula holds as long as all the particles are evenly distributed over the diameter of the tube. Usually more particles are found towards the centre. Also differences in flow speed between the centre and wall give differences in the deposition. All three models (diffusion, sedimentation and impaction) that will be presented here will not consider these problems so that the complete lung model will be build on the same assumptions. A more elaborated formula was given by Ingham [2.9]:

$$\begin{aligned} C &= \frac{8\alpha}{\sqrt{\pi}(1+\alpha)}\left[\frac{2\Delta(1+\alpha)}{\alpha}\right]^{1/2} + \ldots \\ &\ldots \left\{2\frac{4-5\alpha}{1+\alpha} - \frac{16(1+\alpha)}{3\sqrt{\pi}(1+\alpha)}\right\}\left[2\frac{\Delta(1+\alpha)}{\alpha}\right] \\ \Delta &= \frac{k \cdot T \cdot \Delta t}{3\pi\eta d 2W^2} \\ u_a &= \frac{2U}{1+\alpha}\left[1 - (1-\alpha)\frac{W_a^2}{W^2}\right] \end{aligned} \tag{2.7}$$

This formula takes in account the difference in flow speed between the centre of the tube and the wall. The factor α is the slip-factor, giving the flow pattern u. For $\alpha = 0$ there is no slip and the flow pattern is the normal laminar one. For $\alpha = 1$ there is total slip which corresponds to a flat velocity profile (plug flow). This formula should be used in combination with more elaborate models for the sedimentation and impaction.

From (2.5) it can be seen that the diffusion rises with falling particle diameter. So smaller particles will have a higher chance of diffusing toward the walls of the tubes. There is also a time dependence (eq. (2.6)), the shorter time the particle takes to travel through the lung the smaller the distance it will have diffused away from its original streamline and thus a lower deposition probability.

2.3.2 Sedimentation

Sedimentation is the process caused by gravity; all particles of diameter d and specific gravity ρ, experience a pull from gravity (g):

$$F_g = \tfrac{1}{12}\pi d^3 \cdot \rho \cdot g \tag{2.8}$$

Combining this with the air-resistance (2.3) gives that ultimately all particles are moving in the direction of g with a speed:

$$v_s = \frac{2d^2 g}{3\nu} \tag{2.9}$$

which is also known as the settling speed.

Particles that move through a tube without gravity (diffusion is left out for this part of the discussion) will sweep through the inner volume of the tube. Under the influence of gravity this sweep–through volume will deform in the gravity direction (see fig. 2.4). The deposited fraction is simply the fraction of the sweep though–volume that falls outside the tube. The sedimentation distance $v_s \cdot \Delta t$ is small compared to the tube diameter so it is sufficient to correct the sedimentation distance for the gravity angle i.e.:

$$d_{sed} = v_s \cdot t \cdot \cos\alpha \tag{2.10}$$

The sedimentation fraction is the difference between the two overlapping circles in fig. 2.4 and equals for a tube with width W:

$$S = 1 - \frac{2}{\pi}\left(\arccos\left(\frac{v_t t \cos\alpha}{W}\right) - \frac{2v_t t \cos\alpha}{W}\right) \tag{2.11}$$

This again holds if the particles are uniformly distributed.

The settling speed is higher for larger particles, and hence the sedimentation fraction will be higher for larger particles. This effect is opposite to the diffusion and makes that there is an optimum between these two. The sedimentation is maximum in a horizontal tube ($\cos\alpha$ is maximal there). With many tubes in one generation under all possible angels, the gravitation angle takes a cosine like distribution. The sedimentation can than be calculated for the whole generation with the average gravitation angle.

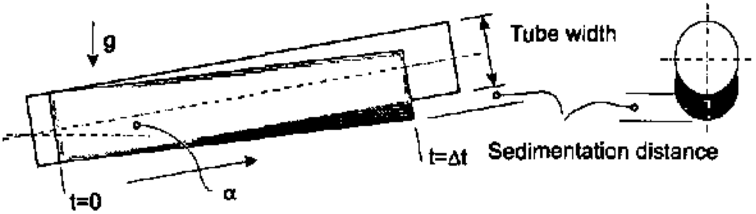

Figure 2.4: *Schematic view of sedimentation deposition*

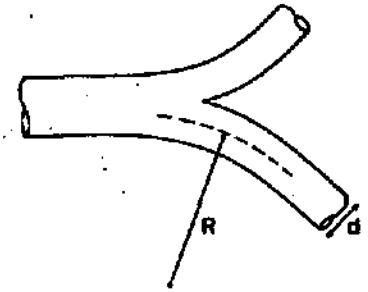

Figure 2.5: *Simplified view of a bifurcation [2.3]*

2.3.3 Impaction

At every bifurcation the tubes, and thus the airstream, make a certain angle. While making this angle the particles experience a certain acceleration. The only force available to keep the particles on the stream line is again the friction force (2.3). A simplified geometry of a bifurcation is shown in fig. 2.5. Outwards pointing from the streamline is the centrifugal force [2.10];

$$f_c = mr\omega^2 \tag{2.12}$$

In which m is the mass of the particle and r the radius to the origin of the rotation. ω —the angular rate— can be expressed in the bending radius (R) and flow (q) as:

$$\omega = \frac{\pi d^2}{4Rq} \tag{2.13}$$

If this centrifugal force is used in (2.9) instead of the gravitational force, we get for (2.11):

$$\begin{aligned} I &= 1 - \frac{2}{\pi}\left(\arccos\left(\frac{v_I \cos\alpha}{W}\right) - \frac{2 v_I t \cos\alpha}{W}\right) \\ v_I &= m\, r \left(\frac{\pi d^2}{4 r q}\right)^2 \end{aligned} \tag{2.14}$$

Which is now the impaction deposition in a certain bifurcation. The bending radius R, was replaced by the bifurcation angle (α). Both the bifurcation angel and R were taken from [2.3].

Also the impaction rises for larger particles, but now also a flow speed dependence can be seen, for higher flow the impaction is higher. This is contrary to the two previous mechanisms (diffusion and sedimentation).

2.4 Lung-Modelling

Direct measurement of particle deposition is possible by using radioactive labelled particles and looking at the radioactive emission from the patient. An other possibility is using a salt solution that is fast cleared from the body. Both methods are inaccurate and quite demanding on the patient. To overcome this, various lung models have been built, both as physical model as well as computer models. Some of the physical models are used as industry standards to validate the output of pressurised canisters aerosol generators. They are mostly fixed representations of only one lung configuration, which limits their use for research.

Computer models have the advantage that every deposition mechanism can be studied separate from all other effects and under all thinkable circumstances. The problem is to get an accurate representation of the real world problem; a computer model is limited by the information provided by its programmer.

Computer models have been made to calculate the deposition of various kinds of particles; industrial dust particles (radioactive radon, diesel exhaust, asbestus etc.), pollen or aerosolised medicine, where the interest is mostly in the total deposited dose. Certain groups are working on improving the modelling and calculation method itself [2.11, 2.12]. Others try to improve the models of the behaviour of the particle in the lung environment. For instance G. Ferron *et.al.* [2.13] reported on their study of the behaviour of hygroscopic particles in the human lung.

2.4.1 Literature results

Before looking at literature results it is important to note what it is we are interested in. The aerosol has to be transported into the deep lung and be deposited there. Most reported models were made for toxic particles and look at the total lung deposition versus the particle size, no distinction is made for the deep lung.

D.A. Edwards [2.14] used a filter approach to model the lung and calculate the total lung deposition of particles. His model uses the Weibel 'A' geometry and takes in account the axial movement of the aerosol. The model is made in an analytical way and final calculations were done using a computer. His main results are presented in table 2.4. They are the total deposition in a healthy lung of small particles. The minimum total deposition was found at 0.4 μm with a deposition between 10 and 20% depending on the breathing pattern.

W. Hofmann and L. Koblinger presented similar results from a Monte-Carlo type simulation [2.11]. The model here is build on the Horsfield lung model. Monte-Carlo simulation was used to express the inter- and intra-patient variations.

Hofmann and Koblinger present in the parts I and II [2.16, 2.17] of their series of articles more detailed data on the lung modelling and also on regional deposition. W. Stahlhofen et.al [2.18, 2.19, 2.20] did measurements on reginal deposition which were fitted to the curves of M. Egan et.al. [2.21]. They distinguish between the slow and fast clearing regions of the lung. This referrers to the clearing of mucus. Up to generation 17 the mucus is fast clearing, which means it is transported rather fast to the trachea. In this way the human lung is able to clear itself from deposited particles (for instance dust). There is no mucus transport from the 17th to 23rd generation, any deposition there has to be removed by the blood stream. This is a slow process for solid particles, hence the name slow clearing region. Of interest for us is the slow clearing fraction i.e. the fraction that is deposited in the slow clearing region. Main results are shown in table 2.5. These results are complementary to the ones in table 2.4 because they give the size of particles that have the maximum deposition in the respiratory region.

From this data it can already be seen that the particles that have the highest deposition rate in the respiratory region are bigger then the ones with the lowest transport loss. These calculations were done on only a few breathing patterns and no effort was done to see how deposition in a certain area could be maximised.

***Table 2.4**: Key results on total deposition from D.A. Edwards [2.14] and W. Hofmann and L. Koblinger [2.15]. V_t; tidal volume, Q; flow, Min size; particle size at which the minimum deposition occurs, Min %; percentage of particles deposited at this minimum, Deposition of 5 μm; percentage of 5 μm diameter particles that gets deposited.*

V_t (mL)	Q (mL/s)	Min size (μm)	Min %	deposition of 5 μm	remark
510	250	0.4	20	70 %	[2.14]
510	250	0.4	10	70 %	improved [2.14]
1085	500	0.4	25	80 %	[2.14]
500	250	0.5	12	90 %	[2.15]
100	250	0.5	20	100 %	[2.15]

***Table 2.5**: Slow clearing fraction of the total lung deposition. V_t; tidal volume, Q; flow, top size; particle size that has the maximum deposition in the slow clearing region, top %; percentage of particles deposited in the slow clearing region.*

V_t	Q	top size	top %	remark
1000	250	4.7	60	[2.21, 2.18, 2.19, 2.20]
1500	750	4.0	55	[2.21, 2.18, 2.19, 2.20]
500	250	6.0	35	[2.21, 2.18, 2.19, 2.20]
250	250	7.0	12	[2.21, 2.18, 2.19, 2.20]
1000	555	2.0	50	[2.17]

2.4.2 Our lung model

To overcome the limitation of the other models, no specific information on local deposition, data only available for a healthy lung and for a few breathing patterns, we made our own model. The geometrical data from Weibel was used together with the deposition formula's presented in the previous paragraphs (formula's 2.6, 2.11 and 2.14). Particles that manage to pass the 17th generation are considered deposited and bio-available. This means that none of the particles is exhaled again. Later on it will be shown that this assumption is valid under certain circumstances.

The calculation method used is finite time stepping. For every time step the airflow and deposition are calculated. The driving part is the breathing which gives the total inhalation flow and total lung volume. Tube diameters are scaled to achieve this total volume. A proper way of arriving at the 'configuration' of the lung for a certain lung volume is to scale the diameters with the square of the volume factor (the current volume over TLC) and the lengths linear with the same factor [2.22]. This procedure is rather crude and more sophisticated procedures exist but only minor changes can be expected [2.23]. The flow speed is calculated for every generation by simply dividing the total inhalation flow by the number of tubes in the generation times one tube's area. With the scaled diameters and flow speed the sedimentation and diffusion can be calculated. The impaction is also calculated for every time step. All this information is stored on disk. The deposition is now known as function of time and place. The sedimentation and diffusion data are integrated over the time path taken by the particles through the 1st to 17th generation, to give the transport loss. The impaction is taken every time a particle passes from one generation to the next. This is repeated for all particle diameters of interest. Breathing pattern (breathing frequency, flow variation) and characteristic lung volumes (FRC and Tidal volume) are external parameter to the programme.

The model uses only one ideal lung morphology (from table 2.1) but should do predictions for a whole population. This can be achieved by varying the sizes given and looking at the influences of these changes. This wasn't done yet, but could be part of further research. Secondly does the model describe a healthy lung while the aerosol particles will be transported through a diseased lung. To look at the differences between the healthy and diseased lung we used the morphological data from Kim (table 2.3) to model a diseased lung.

2.4.3 Results

First the transport loss (e.g. deposition in generations 1 to 17) under different breathing conditions will be considered. The transport loss is always taken as the fraction that is deposited before the 17th generation. Secondly the place where particles are deposited and deposition mechanism responsible for this will be investigated.

Fig. 2.6 shows the basic transport loss curve for a male under normal breathing (c.f. table 2.2). Clearly can be seen that there is an optimum particle size around 2 μm and that sedimentation is the main deposition mechanism as the particles get bigger. If we now compare this graph with the one for a male at exercise (fig. 2.7), it can be clearly seen that here the transport loss is lower. This is mainly due to the fact that there is less time for sedimentation and the impaction did not rise appreciable yet. Fig. 2.8 shows that the main deposition mechanism for 2 μm particles is diffusion and that most of the lost particles are deposited towards the lower airways. This can be explained by the lower flow speed and thus longer residence times of the particles in these generations. The impaction has a maximum around the 3rd generation.

For a female (see fig's. 2.9, 2.10) the same effect can be seen; a lower transport loss under the exercise condition. Again the optimal particle size did not change appreciably. Table 2.6 summarises the results for all age groups.

Table 2.7 summarises our the calculation results for the obstructed lung. The graphs are not substantially different from the ones shown before (fig's 2.6 to 2.10) so they are omitted. The same tendency can be seen, a smooth varying function that has an optimum in the 1 to 1.5 μm region. The optimal size is slightly smaller then what was seen for the healthy lung. Remarkable is that impaction is the main deposition mechanism in the obstructed regions. Which can be understood by the higher flow rates in these regions.

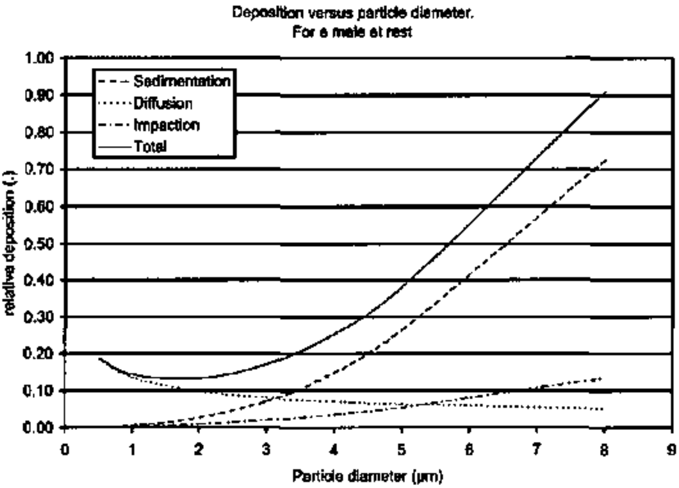

Figure 2.6: Transport loss in generations 1 to 17, for a male at rest.

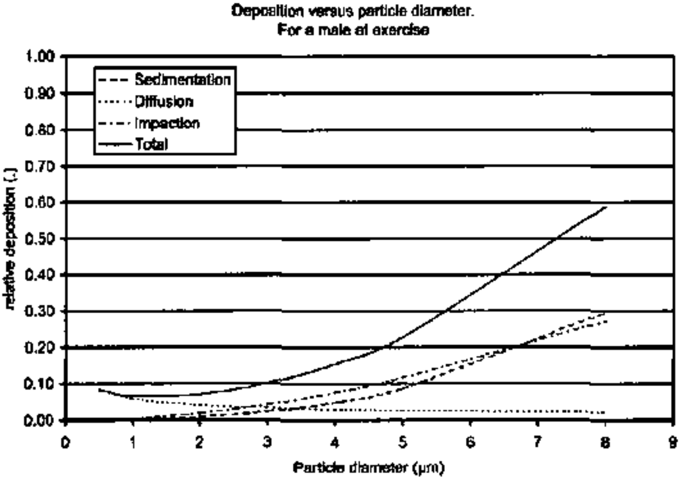

Figure 2.7: Transport loss in generations 1 to 17, for a male at exercise conditions.

2.4.4 Conclusion and discussion on particle size

Particles of 1 to 1.5 μm are transported the deepest in the lung with the lowest loss in generations 1 to 17. The highest deposition occurs always toward the highest

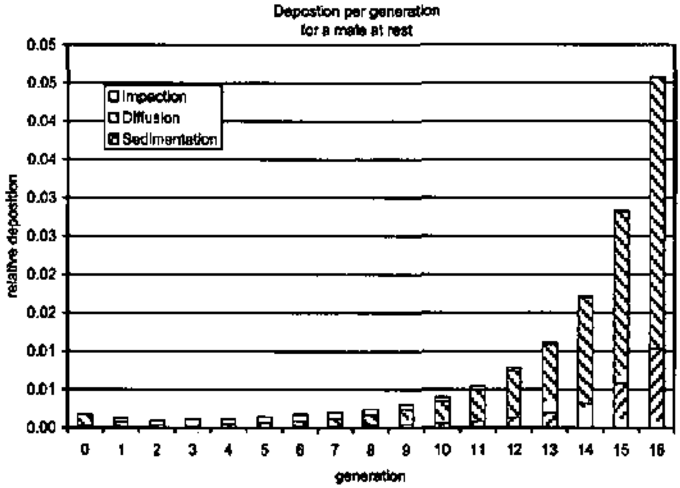

Figure 2.8: *Loss per generation for 2 μm particles in a male at rest. Impaction is the main deposition mechanism for the higher generations, for the deeper ones diffusion becomes stronger due to the longer residence times.*

generations. Particles of 8 μm diameter have under most circumstances a 100% transport loss before generation 17. Finally, it can be seen that the loss in reasonable as long as the particles stay below 5 to 6 μm. For medicine application, particles should not reach into the alveoli but get as close to them as possible [2.2]. From fig. 2.11 the difference between 2 and 4 μm particles can be seen. The 4 μm deposit 100% before the alveoli but still deep into the lung. This together with the largest size that can be transported through the lung puts the size window at 4 to 6 μm diameter.

Impaction did not play an important role in the deposition, contrary to what is expected from literature. This can be understood by the following. The models for diffusion and sedimentation are worst case models, due to the assumption of a flat particle distribution. They will thus give the maximum possible deposition value and in reality a lower deposition can be expected. The impaction model is a best case model; the flow stays laminar and only centrifugal force causes

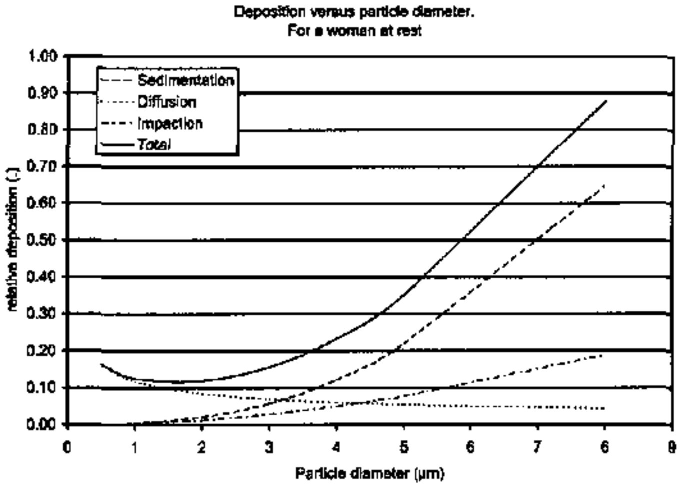

Figure 2.9: Transport loss in generations 1 to 17, for a female at rest.

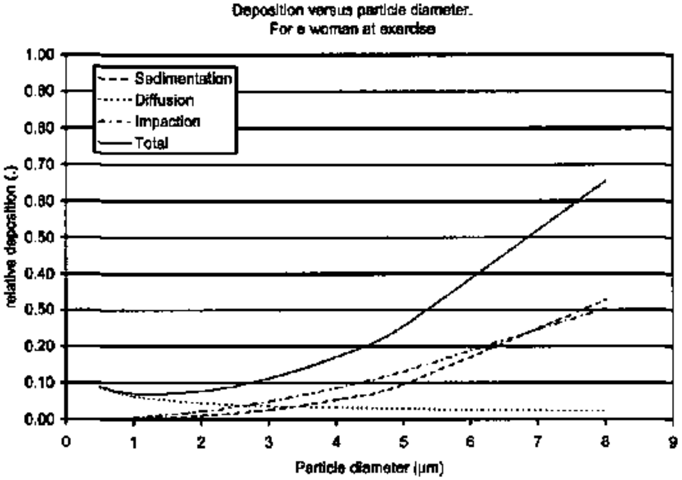

Figure 2.10: Transport loss in generations 1 to 17, for a female at exercise conditions.

deposition. In reality all kinds of small turbulences can be expected, raising the deposition probability. Combining these two will overestimate the diffusion and sedimentation and underestimate the impaction.

For an asthmatic's lung can be said that the transport loss is comparable with a

*Table 2.6: Optimal particle size to reach into the deep lung, for the typical breathing patterns (table 2.2. The first line is under normal breathing conditions and the second under light exercise. * Our lung model did not work for the 5 year old due to problems with the scaling procedure.*

	height (cm)	Optimal size	Loss %
male	176	2.0	13
male	176	1.2	6
female	163	1.8	12
female	163	1.2	7
15y male	169	1.8	12
15y male	169	1.0	7
15y female	161	1.8	11
15y female	161	1.1	7
10y	138	1.4	10
10y	138	1.0	6
5y	110	*	
5y	110	*	

Table 2.7: Transport loss in generations 1 to 17 with obstruction of airways as seen in an asthmatic (first and second column); obstructions according to Kim [2.7]. Lung geometry and breathing pattern for a male at exercise were used. Optimal size is the size with the lowest loss.

generation	obstruction in gen. (%)	optimal size (μm)	loss %
3	25	1.2	7
3	40	1.1	7
0–3	25	1.2	7
4–7	25	1.1	7
0–7	25	0.7	4

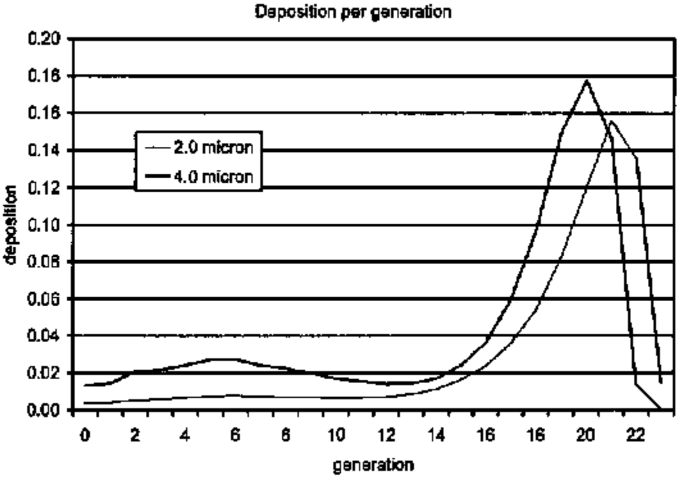

***Figure 2.11**: Deposition per generation for 2 and 4 μm diameter particles. The 4 μm particles do not reach all the way into the alveoli and are therefor better suited for IDT then the smaller ones.*

healthy one. The transport loss is higher for the slightly larger particles of 6 μm. A low inhalation flow seems to be favourable to minimize the loss due to impaction in the obstructed region.

2.5 Medicine Dose and Properties

Depending on the type of medicine certain area's of the lung should be targeted for deposition [2.2]. The discussion so far focussed on the distal airways and the alveoli. For asthma medicine, that interact with the muscle tissue inside the lung, the alveoli should be avoided. From the previous results it can be clearly seen that to target higher in the lung the droplets should be bigger then the ones with the lowest transport loss. With rising particle size also the mouth and trachea deposition will rise, which is an unwanted effect. More experimental data is necessary to conclude if this is a major problem.

From Fig. 2.11 it can be deduced that the $2\mu m$ particles have a loss of 13%

up to generation 17 and the $4\mu m$ a loss of 30%. The loss of $4\mu m$ is considerable but still better then the traditional inhalers. It is necessary to work at this higher diameter to prevent particles from depositing in the alveoli.

The demands set out by the Food and Drug Administration (FDA) for IDT devices are published in the guidance documents for industry [2.24]. Here it is written that the ejected volume of 10 doses out of 10 must be within ±25% of the label claim. Further, 9 out of those ten doses must be within ±20% of the label claim. They do not set demands for the actual dose because this is medicine and treatment dependent. A typical dose from a spray can type device is 15 to 20 μl which is ejected in about 1 to 1.5 s. This means that we have to construct a device that vaporises 10 to 15 μL of medicine per s.

The medicine itself is usually a mixture with or suspension in, water or ethanol. For the research only the carrier liquid will be used, first of all for safety reasons. Water also has rather ideal properties for use in drop on demand devices. Only a limited number of parameters change with a different liquid, once the device is fully characterised and optimised for one particular liquid.

2.6 Conclusion and discussion

The lowest particle loss and thus the deepest penetration was seen for particles between 1 and 1.5 μm diameter. For targeting the deep lung, but avoiding the alveoli the ideal size range was found to be 4 to 5 μm. Most important to note is that for all age groups a lower deposition was calculated under light exercise conditions. The ideal particle size was also smaller for this situation. The ideal droplet size with respect to the manufacturing is always the largest possible for several reasons:

- The smaller the droplets the more they will deposit in the alveoli, something we want to prevent. Slightly bigger droplets will guarantee deposition in the distal airways, towards but not in, the alveoli.
- Diffusion becomes more and more important as deposition mechanism for smaller particles. To arrive at complete deposition of the particles breath-

holding will be necessary.

- The volume per droplet is eight times higher if we can double the diameter. This means that we need a lower frequency and lower number of nozzles to arrive at the same total flow.
- The deposition changes only slowly around the optimum so moving away from the optimum will only marginally influence the transport loss.
- Power consumption will be lower when generating bigger droplets due to lower total surface build up and lower flow resistance in the nozzle (see chapter 3).

For particles larger then the optimum size the main deposition mechanism is sedimentation. For higher flows the impaction will have the same order of deposition loss. For these particles the main deposition can be observed in the last few generations before the respiratory zone. For the obstructed lung only a slight change in optimal particle size was seen but the influence of impaction became more important.

The influence on the ejection time was not considered yet; the total deposition was calculated over the whole inhalation period.

The classical spray-can has quite a large portion of its total output *volume* in the range above 6 μm, which will be largely lost during transport.

The extra-thoracic losses were neglected so far. From literature it can be seen that most loss in this area is due to ballistic deposition and not so much for the other mechanisms used in the lung model. A properly designed inhaler will prevent this ballistic losses by ejecting droplets with a very low speed so that they immediately are taken into the air stream. Considering that the airstream at the mouth is 1 to 2 $m/_s$, this means that the droplets should be ejected with a lower speed.

2.7 Further work

There are still a number of unknown factors that are not in the current lung model. For instance the hygroscopic growth of the droplets or the evaporation of the carrier liquid, which will make the droplet grow or shrink. Also the extra-thoracic losses were neglected. The final optimum size for the 'smart–inhaler' will have to be found by clinical trials. Finally with a properly designed device it will be rather simple to changing the average size of the droplets in the generated aerosol by changing the production parameters of the device. For the remainder of the research the goal will be set to arrive at 4 to 5 μm diameter with a low dispersion, which will be a good starting point for further fine tuning.

Bibliography

[2.1] E.R. Weibel. *Morphometry of the human lung*. Springer Verlag, 1963.

[2.2] P. Zanen. Targeting drug aerosol to the airways, 1999. to be published.

[2.3] K. Horsfield, G. Dart, D.E. Olson, G.F. Filley, and G. Cumming. Models of the human bronchial tree. *J. Applied Physiolology*, 31(2):207–217, 1971.

[2.4] J.B. West. *Respiratory physiology*. Williams and Wilkins, London, 3 edition, 1985.

[2.5] P. Zanen. *Aerosol formulation and clinical efficacy of bronchodilators*. PhD thesis, Universiteit Utrecht, Faculteit geneeskunde, 1999.

[2.6] Bergmann. private communications, 1999.

[2.7] C.S. Kim, L.K. Brown, G.C. Lewars, and M.A. Sackner. Deposition of aerosol particles and flow resistance in mathematical and experimental airway models. *J. Appl. Physiol*, 55:154–163, 1983.

[2.8] L.D. Landau and E.M. Lifshitz. *Fluid Mechanics*, volume 6 of *Course of theoretical physics*. Pergamon Press, Oxford, 2 edition, 1987.

[2.9] D.B. Ingham. Diffusion of aerosols from a stream flowing through a cylindrical tube. *J. Aerosolsci.*, 6:125–132, 1975.

[2.10] H. Goldstein. *Classical mechanics*. Addison Wesley, Reading, Mass., USA, 2 edition, 1980.

[2.11] L. Koblinger and W. Hofmann. Analysis of human lung morphometric data for stochastic aerosol deposition calculations. *Phys. Med. Biol.*, 30(6):541–556, 1985.

[2.12] J.W. Gentry and N.C. Liu. Methods for predicting total dependent particle collection efficiencies with more then one mechanism acting. In *Aerosol inhalation: recent research frontiers*, pages 205–213, 1995.

[2.13] G.F. Ferron and B. Bush. Deposition of hygroscopic aerosol particles in the lungs. In *Aerosol Inhalation: Recent Research Frontiers*, pages 143–152, 1995.

[2.14] D.A. Edwards. The macrotransport of aerosol particles in the lung: Aerosol deposition phenomena. *J. Aerosol Sci.*, 26(2):293–317, 1995.

[2.15] W. Hofmann and L. Koblinger. Monte-carlo modelling of aerosol deposition in human lungs. part iii: comparison with experimental data. *J. Aerosol Sci.*, 23(1):51–63, 1992.

[2.16] W. Hofmann and L. Koblinger. Monte carlo modelling of aerosol deposition in human lungs. part i: Simulation of particle transport in stochastic lung structures. *J. Aerosol Sci.*, 21(5):661–674, 1990.

[2.17] W. Hofmann and L. Koblinger. Monte carlo modelling of aerosol deposition in human lungs. part ii: Deposition fractions and their sensitivity to parameter variantions. *J. Aerosol Sci.*, 21(5):675–688, 1990.

[2.18] W. Stahlhofen, J. Gebhart, and J. Heyder. Experimental determination of the regional deposition of aerosol particles in the human respiratory tract. *Am. Ind. Hyg. Assoc. J.*, 41:385–398, 1980.

[2.19] W. Stahlhofen, J. Gebhart, and J. Heyder. Biological variability of regional deposition of aerosol particles in the human respiratory tract. *Am. Ind. Hyg. Assoc. J.*, 42:348–352, 1981.

[2.20] W. Stahlhofen, J. Gebhart, J. Heyder, K. Philipson, and P. Camner. Intercomparison of regional deposition of aerosol particles in the human respiratory tract and long-term elimination. *Exp. Lung Res.*, 2:131–139, 1981.

[2.21] M.J. Egan and W. Nixon. Dn the relationship between experimental data for total deposition and model calculations part ii: Application to fine particle deposition in the respiratory tract. *J. Aerosol Sci.*, 20:149–156, 1989.

[2.22] C.P. Yu and C.K. Diu. *Am. Ind. Hyg. Assoc. J.*, 43:54–65, 1982.

[2.23] W. Hofmann. Lung morphometry and particle transport and deposition, overview of existing models. In *Aerosol inhalation: recent research frontiers*, pages 91–102, 1995.

[2.24] FDA. Guidance for industry; metered dose inhaler (MDI) and dry powder inhaler (DPI) drug products. http://www.fda.gov/gder/guidance/index.htm, 1999.

Chapter 3

Design of the vaporiser

Abstract

This chapter describes the design process of the vaporiser. A survey of possible designs was made and a preferable design was chosen. First results showed that it is possible to build a droplet generator which works with drop on demand in the right size range and has sufficient throughput. DRIE was chosen to etch the nozzles through a thin membrane. Making the actual nozzle as short as possible minimizes the fluid resistance and thus the power consumption of the device. A 10 x 10 mm^2 *device is fabricated and tested.*

3.1 Introduction

It was already seen that the droplets in the aerosol should fall within a very narrow size range to be able to target the deep lung. It was also seen that an active vaporiser element is preferable to be able to use breath control. Current aerosol generators perform poorly in that sense, they produce a broad size range of droplets and they are manually activated. This chapter will go through the possibilities of constructing an aerosol generator that performs better then the current pressurised canister devices, using micro-fabrication techniques. The possible techniques will ultimately have to be judged on applicability with respect to the next demands:

- Controllable and mono dispersive aerosol generation.

- Sufficient throughput.
- Start/stop characteristics.
- Power consumption.
- Batch processable.
- Low cost of production.

The first three of these demands were already mentioned in the introduction and chapter 2. The last two are added here because they are pure fabrication demands. The cost aspect is of course important for future commercialisation but is not of major importance in this early stages.

The first choice for the inhaler system is the aerosol generation method, which will put out the major components of the system. Current devices for uniform (mono-dispersive) droplet generation can be found in ink-jet printers. Their droplet size is somewhat larger then our target range of 4 to 5 μm; the lowest size reported is 30 μm [3.1]. The uniformity though is usually very good and of the order of several micron bandwidth [3.2].

To arrive at sufficient throughput in the right size range many droplets need to be generated, c.f. table 3.1. Table 3.2 gives the number of nozzles and frequency for 5 μm droplets to arrive at sufficient flow. Consequently, the maximum ejection frequency of several kHz for normal ink-jet devices is too low for our application. For an ink-jet printer it is also important to be able to address every nozzle separately. This means that each nozzle has its own actuator. For our application this is not necessary and it would complicate the system unacceptably. This means that the same basic techniques can be used but that the droplet generator will be a completely new device.

A survey was made, taking existing ink-jet systems as starting point. Two other aerosol generation techniques using micro-technology will also be investigated. Their merits will be summarised in the next paragraphs and their applicability for an aerosol generator will be investigated.

3.2 Aerosol generation methods

There are different ways of generating an aerosol using an active element. Four different techniques will be introduced in the next paragraphs: surface waves, jet-breakup, drop on demand and electro-spray. Surface waves will generate an aerosol with a distribution of sizes more or less comparable to the spray-can devices. The next two, jet-breakup and drop on demand, generate a mono-dispersive aerosol. As last electro-spray is mentioned to complete the list, it is suitable for both poly- and mono-dispersive aerosol generation

3.2.1 Surface waves

Surface or capillary wave device were reported for possible application in drug delivery but also for perfume dispensing. Kurosawa *et.al.* [3.3, 3.4] reported on devices made with micro-technology. During operation a thin sheet of liquid is

Table 3.1: *Droplet diameter and volume. The last column gives the number of droplets necessary to arrive at 20 μl.*

diameter μm	volume μL	total number
100	0.00052	3.82E+04
50	6.54E-05	3.06E+05
10	5.23E-07	3.82E+07
5	6.54E-08	3.06E+08
2	4.18E-09	4.78E+09
1	5.23E-10	3.82E+10

Table 3.2: *Number of nozzles and frequency to arrive at 20 $\mu l/s$*

Droplet volume fL	Frequency kHz	Number of nozzles (.)
65	1	$310 \cdot 10^3$
(=5μm diam.)	10	$31 \cdot 10^3$
	100	3100
	200	1550

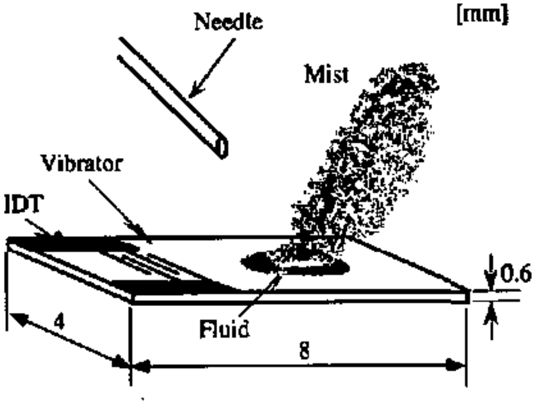

Figure 3.1: Typical surface acoustic wave device [3.4]. Dimensions in mm.

flown over an ultrasonically vibrating surface which causes capillary waves. These waves can pinch off and so form a mist of small droplets. Instead of a vibrating bottom also a lambda wave can be used (see fig 3.1). The basic result stays the same.

The dispersion of droplet size is large, as can be seen from fig. 3.2. The peak lies around 3 μm but larger droplets make op a large portion of the total volume. For comparison, one droplet of $10 \mu m$ diameter hold the equivalent volume of eight 5 μm diameter droplets.

The device is rather simple in construction and very rugged. It has also the possibility to be easily mass produced. The devices reported in literature that used this principle had a rather high power consumption; for 20 $^{\mu L}/_{s}$, more than 2W were needed. Hence this device is not ideal for our application, and will not be further pursued.

3.2.2 Jet-breakup

A pressurised fluid reservoir that is connected with a nozzle will issue a liquid jet. After a certain distance this jet will break-up into individual droplets due the

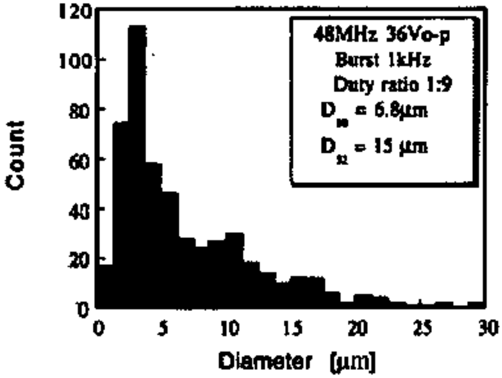

***Figure 3.2**: Distribution of particle size as measured from a surface wave device. A major part of the total volume sits in the bigger particles. [3.4]*

Rayleigh instability [3.5]. This process is comparable with what can be observed with a slow running tap. Small perturbations on the diameter of the jet are instable and will grow in time, finally causing the breakup. If the perturbations are made by modulating the pressure behind the nozzle in a regular manner so will the jet break up in a regular manner. A very low modulation amplitude is sufficient, so apart from a supply pressure there is very little energy demand in such a system. A schematic drawing of a jet break-up system is shown in fig. 3.3.

The size of the generated droplets can be easily influenced by changing the modulation frequency. The higher the frequency (f) the shorter the pieces in which the jet breaks up and so the smaller the droplet volume. Hence the droplet volume is inversely proportional to the actuation frequency:

$$V_{drop} = \frac{Q}{f_{actuation}} \tag{3.1}$$

Q, the total flow out of the nozzle, is fixed by the supply pressure and the flow resistance of the nozzle. There is a lower and upper limit to the actuation frequency. When the actuation frequency is too high the droplets are generated so close to

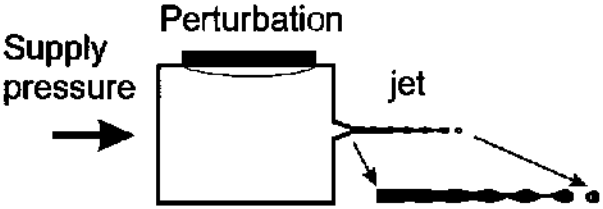

Figure 3.3: *Schematic of a jet-breakup system. The supply pressure pushes the liquid as a jet out of the nozzle. Due to the regular perturbation the jet will break up in regular pieces.*

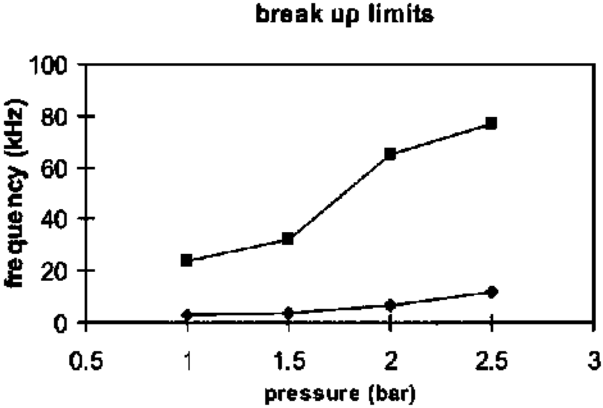

Figure 3.4: *The limits between which the jet breaks-up in a regular fashion. When the actuation frequency is too low, chaotic breakup will occur. For a too high frequency the droplets will not be able to separate.*

each other that they touch and again form a jet. When the actuation frequency gets too low, the chaotic break-up takes over again. Fig. 3.4 shows the experimentally determined frequency limits for different supply pressures for a $70\mu m$ nozzle.

On a system level this devices is less favourable because it is not easy to start and stop the generator. It needs external valves to switch on the supply pressure. This complicates the system and introduces an extra component. Fig. 3.5 shows a system with all its external components.

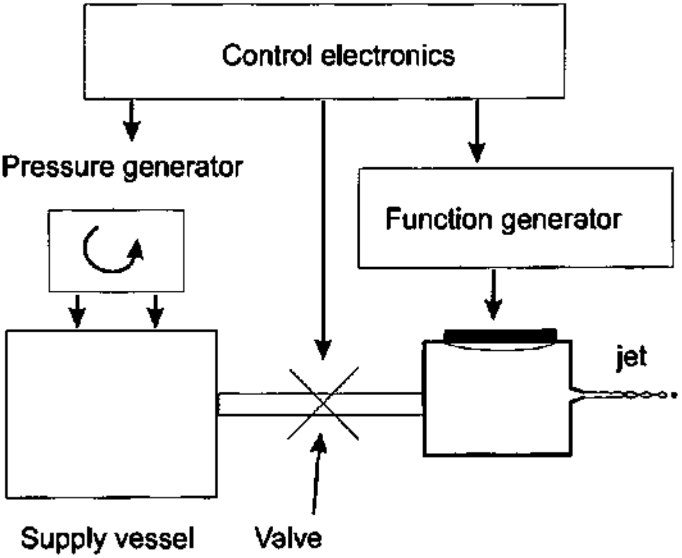

Figure 3.5: The jet-breakup inhaler with all its external components

3.2.3 Drop on demand

Drop on demand (DOD) is widely used in ink jet printers. It needs apart from the droplet generator no further active components and usually gravity suffices to refill the fluid chamber after droplet ejection. The same actuator that is used to modulate the pressure in the jet-breakup system can be used but now working at a much higher amplitude. A pressure pulse travels through the fluid chamber towards the nozzle, causing liquid to be ejected. Of importance is the speed with which the pressure is raised. This to give the liquid sufficient kinetic energy to break through its surface tension. Fig. 3.6 shows a time loop of the ejection of the droplet. The main part of the droplet can be seen pulling through the surface tension until pinch off occurs and the actual droplet is formed.

The droplet size is mainly depending on the size of the nozzle but also on the viscosity and the surface tension of the liquid. The exact dependencies are not yet investigated for the droplet size of interest. The drop on demand technique seems

Figure 3.6: *Time loop of the ejection of a single droplet. The nozzle is situated on the bottom of the picture. [3.6]*

the most promising for aerosol applications; it needs no further components and it is easily controlled.

The next paragraphs, 3.3 and 3.4, will go into the different implementations of a DOD system.

3.2.4 Electro-spray

Electro-spray is often used to define and introduce samples in a mass-spectrometry system. It was also the first system used for generating mono-dispersive droplets for medicine administration. P. Zanen [3.7] used such a system for his research into the ideal droplet size because of its narrow size distribution. It also has the possibility of adjusting the droplet size by changing the operation parameters.

The actual system (see Fig. 3.7) consists of a small capillary that is placed over a surface. A high potential is applied and droplets get drawn electrostatically from the capillary [3.8, 3.9]. Depending on the feed parameters (i.e. the pressure in the feed channel to the capillary), the applied potential and the conductivity of the liquid a stable droplet generation can be achieved. The potential necessary is rather high (of the order of 10 to 20 kV) and less suitable for a portable device. A well designed device can have a very narrow size range of generated droplets. By changing the potential, different droplet generation regimes can be addressed; from regular droplets through to an irregular spray.

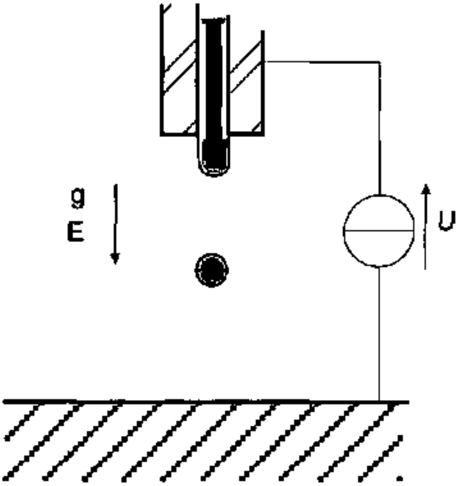

Figure 3.7: *Schematic drawing of an electro-spray system. Depending on the potential between the electrodes a regular or irregular stream of droplets can be generated*

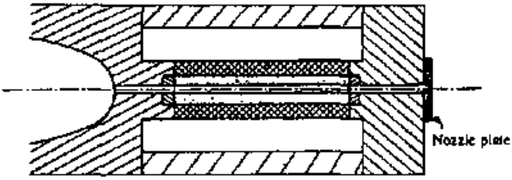

Figure 3.8: *Drop on demand device with a nozzle made from a ruby disk. [3.6]*

3.3 Actuation methods for Drop on Demand

Considering the drop on demand devices there are several different actuation methods possible, i.e. the pressure pulse can be generated in several ways. It can be done by creating a gas bubble inside the chamber, through boiling part of the liquid [3.10, 3.1]. This method is mostly used in ink jet printers nowadays because it gives a very compact actuator design. This method is not of interest for our

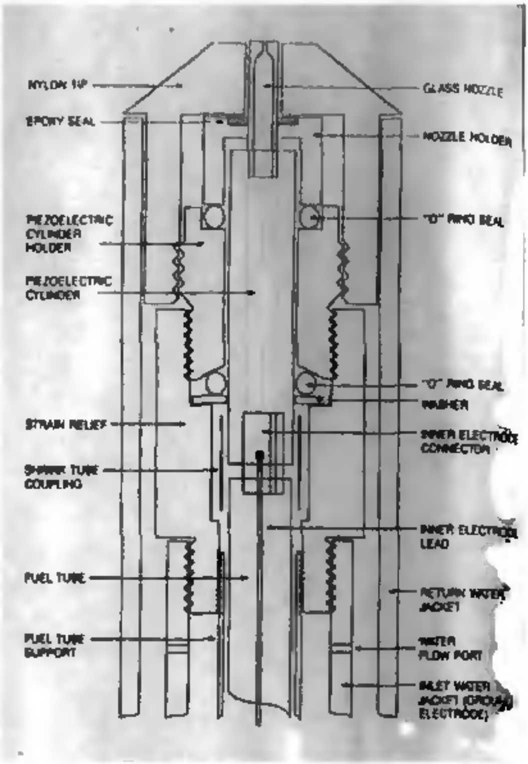

***Figure 3.9**: Drop on demand device using a contracting piezo around a glass capillary. On the end the capillary contracts to form the nozzle. From [3.2]*

device since most medicine degrade at such elevated temperatures. The actuation frequency is also limited to several kHz.

The second method is by changing the geometry of the chamber in some way. Mechanically this can be done by contracting a piezo tube that is placed around the fluid chamber (see fig. 3.8 and 3.9) for round devices. For flat configurations it is possible to buckle a membrane ([3.11], fig. 3.10), or by electrostatically deflecting one side of the chamber [3.12] (see Fig. 3.11). An other method is by making one of the sides a bimorph which deflects under temperature or an electric field. In the last case one of the layers is a piezo material ([3.13], fig. 3.12).

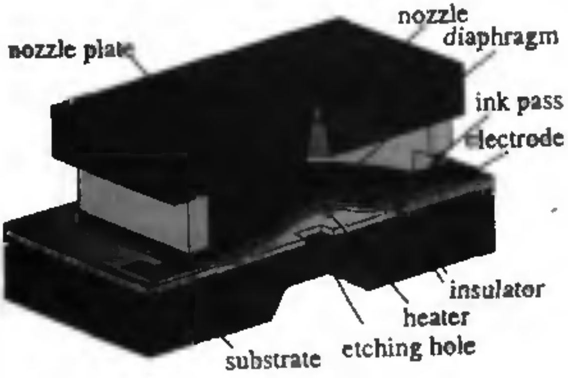

***Figure 3.10**: Drop on demand device actuated with a buckling membrane. Advantage is the high energy available, but it is slow. [3.11]*

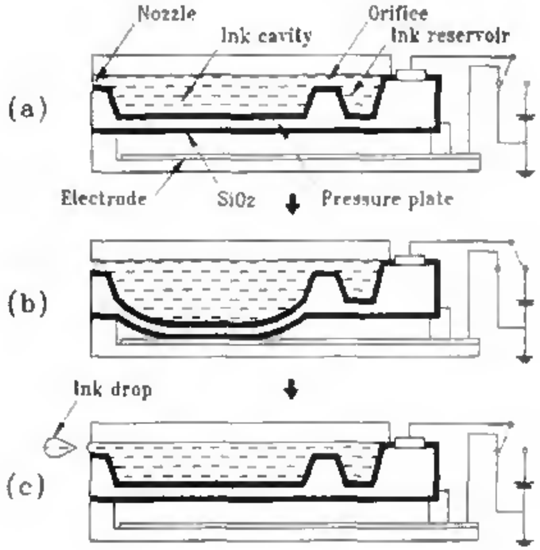

***Figure 3.11**: Electrostatically actuated device, with the droplet ejection cycle. The maximum droplet ejection frequency is 30kHz.*

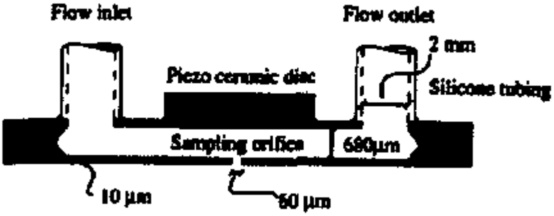

Figure 3.12: *A piezo actuated drop on demand device in a flat configuration [3.13]*

From all these the piezo seems the most promising, there is no temperature effect in the liquid and piezo actuators can be actuated at a very high frequency. A system build with a piezo actuator will only be dependent on the mechanical properties (viscosity and mass) and not so much on the physio-chemical (boiling temperature etc.) of the fluid that is inside the chamber.

3.4 The Nozzles for Drop on Demand

The size of the droplets ejected is mainly depending on the size of the nozzles [3.2]. This means that they are of a main interest for the device design. The device from IBM uses a small ruby disk to define the nozzle, as shown in Fig. 3.8. Systems Research Laboratory demonstrated a device that used a glass capillary as nozzle which was further developed by Microdrop GmbH [3.14] (see also Fig. 3.9). None of the device has the potential to use more then one nozzle at the same time.

When using microtechnology the device will be made in a planar configuration. For a vaporiser the layout has to be such that many nozzles can be accommodated. Nozzles can be made in a planar way by directly etching them in the face of a silicon wafer, hence this is called a face shooter design. The other option is to etch trenches and later assembling these into nozzles, this is called a side shooter (see Fig. 3.14). The side shooter is popular with the ink-jet industry because it is easy to make arrays of fluid chambers and nozzles where every fluid chamber gets its own actuator. Integration density is mostly limited by the size necessary for the fluid

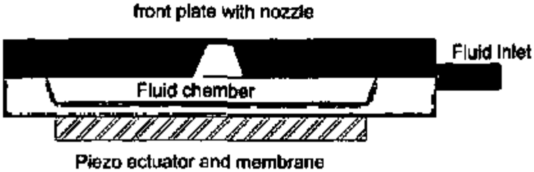

***Figure 3.13**: The basic face-shooter design. Nozzles are etched in one side of the device. The back side is later attached to the front side to form the fluid chamber.*

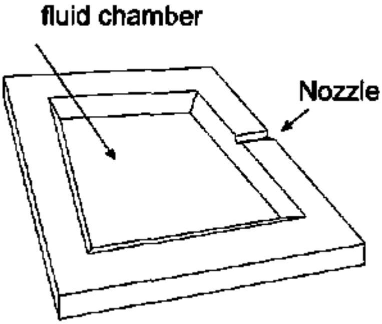

***Figure 3.14**: The basic side-shooter design. Nozzles are formed by etching trenches in one or two sides of the device. The two sides are later assembled to form the nozzles and the fluid chamber.*

chamber/actuator. The device published by W.G. Hawkins [3.15] has 192 parallel working nozzles with a pitch of 84 μm ($\hat{=}$ 300dpi). The accuracy of the nozzles made in a side shooter is mostly depend on mask alignment and mask selectivity in the processing. Especially mask alignment can cause several μm deviation in the channel width and hence the nozzle size. The length of the channel is defined during dicing which again gives an uncertainty. The limited space available on the side of a device and the inaccuracy in the actual nozzle make a side shooter less favourable for our application.

With KOH etching it is possible to define a small hole in a silicon wafer. Here use is made of the anisotropic etching of Si, some crystal planes hardly etch while other etch rather fast. The nozzle will have a pyramid shape and a square opening.

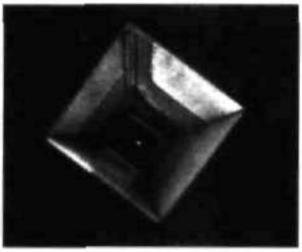

***Figure 3.15**: Image of a KOH etched nozzle hole.*

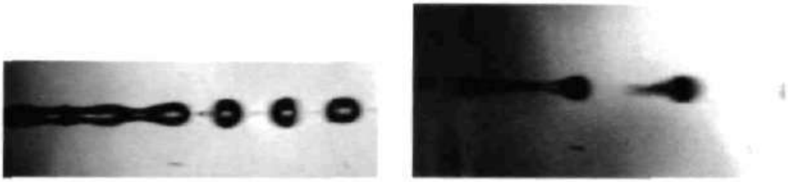

***Figure 3.16**: The two modes of operation for a KOH etched nozzle made in our laboratory. Left the jet break-up mode and right the drop on demand mode. The nozzle size is 70 μm.*

Fig. 3.15 shows a typical nozzle. Etching starts at the backside of the nozzle and terminates at the actual nozzle opening. Critical is here the alignment of the etch mask on the back side of the wafer with the crystal planes of the Si wafer. A misalignment of 0.5° already gives a 10 μm difference in size of the nozzle on the other side of the wafer. Advantage of this type of nozzle is the low flow resistance.

The devices, made in our laboratory, with this type of nozzle functioned both in drop on demand as well as jet break-up mode (see fig. 3.16) With KOH type nozzle a maximum density of 300 nozzles per cm^2 can be achieved. Comparing this with table 3.2 shows that we need a frequency of 400kHz for a 1 cm^2 device or otherwise a 4 cm^2 device for 100kHz actuation. Both of these seem unrealistic so a different nozzle fabrication process has to be found.

Instead of etching all the way through the wafer with the KOH etching, it is also possible to leave a thin membrane and to later etch small holes through these

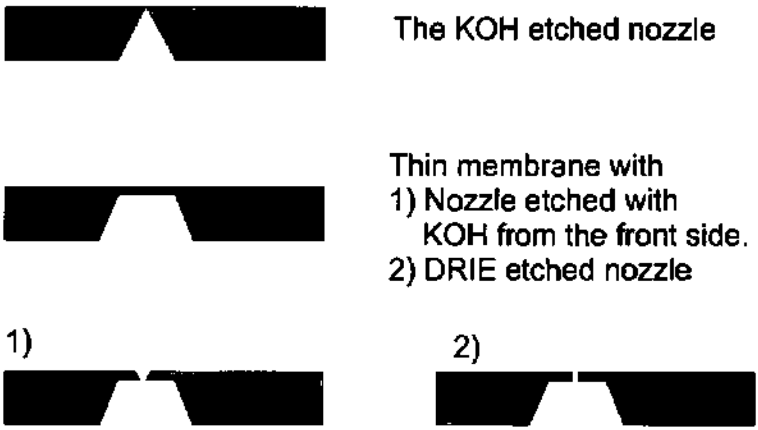

Figure 3.17: *The production sequence for the nozzles etched through thin membranes. The KOH etched ones are pyramid shaped and have thus a low flow resistance. The DRIE etched nozzles are straight and have a very well defined size.*

membranes (see fig. 3.17). When again KOH etching is used to etch through the membranes from the other side the alignment problem will be less. However the membrane thickness now becomes the critical factor. The accuracy for the membrane thickness is given by the initial parallelism of the two wafer faces.

Deep Reactive Ion etching (DRIE) makes it possible to etch nozzles with a vertical wall. The actual thickness of the membrane is no longer a problem, the nozzle size is fixed by the etch mask (see fig. 3.18).

It is possible with either of the two methods to place more nozzles in one membrane. In this way the nozzles can be placed much closer to each other, and hence the density is much higher. We placed a maximum of 1800 nozzles on a 1 cm^2 device.

Contrary to what is usually reported in literature, the limitation for droplet ejection seems to be the total flow resistance in the ejection nozzle in combination with the actuation amplitude and not so much the actual droplet size. By etching the nozzles in a thin membrane the flow resistance can be minimized. The flow resistance can be further minimized by making the nozzles slightly tapered.

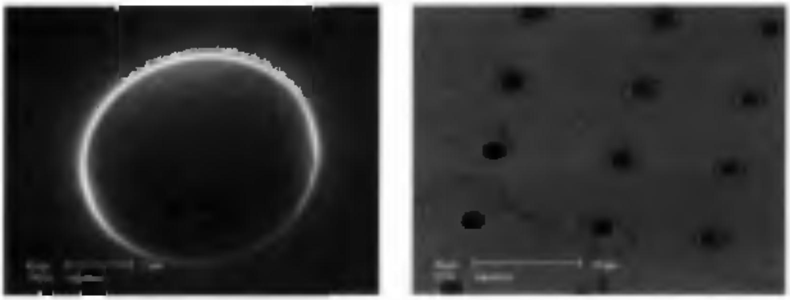

Figure 3.18: The DRIE etched nozzles. *Left: close-up of one nozzle, clearly the smooth, vertical wall can be seen. Right: Surface with several nozzles of different size, used for process characterisation.*

Figure 3.19: *The 3 μm nozzle. An oxide rim was used to better control the droplet ejection. [3.16]*

Further development in our laboratories [3.16], showed that nozzles of 3 μm are possible (see fig. 3.19).

3.5 Assembly techniques

Both the side- and face-shooter design as presented (fig. 3.14) need three assembly steps. The device itself consists of two halves that need to be connected together and then there is the piezo actuator and the fluid connection (see fig. 3.20). Each

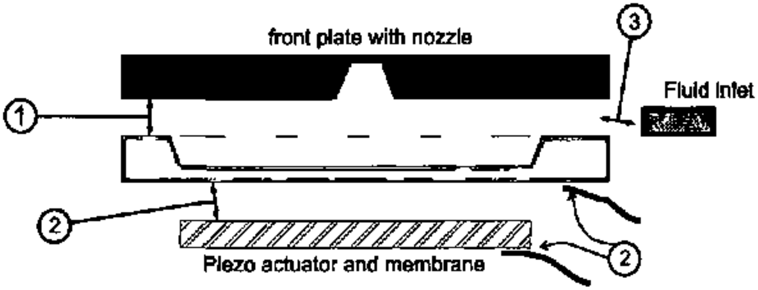

Figure 3.20: The assembly steps; 1) The two device halves are assembled together to form the fluid-chamber. 2) The piezo-actuator and the electrical contacts. 3) The fluid connection.

of these steps has its own specific needs in rigidity and chemical resistance.

3.5.1 The two device halves

The rim between the two device halves not only closes the fluid chamber but also provides the mechanical coupling between the two sides. The connecting medium should be water resistant (or if an other carrier liquid is used against that liquid) and stiff enough to provide the mechanical coupling. The two device halves were mostly assembled using epoxy glue with a high resistance against water (EPO-TEK OE101). The procedure is simple and there is no special surface requirement. Due to its low viscosity the glue fills out all uneven parts that might exist between the two sides. The epoxy glue was cured for 30 min. at 90°C in air.

An other possibility for assembly of these two parts is by sputtering a layer of Pyrex on one of the sides and to use this layer for anodic bonding. Theoretically this type of bond is far more rigid and resistant then the glue bond. Anodic bonding requires perfectly smooth surfaces and a conditioned working environment. The bonding was done at a temperature of 400°C at a potential of 40V. A higher potential caused sparks. With a better design that would prevent a small air-gap at the sides of the device this sparking can be prevented and bonding can be done close to the breakdown voltage of 120V. Bonding took 45min.

The anodic bond is much stiffer as the glue bond so it was expected that the overall quality factor (see also par. 4.2.1, page 63) of the resonances would improve. Tests showed that the quality factor of the complete device did not improve. This is probably due to the epoxy layer between the piezo and the device and the quality factor of the piezo itself which make up the majority of the quality factor. Epoxy glue is the preferred way to assemble the device because of its simplicity in use. Also has the epoxy technique sufficient potential for mass production.

3.5.2 The piezo actuator and the electrical connections

Also the mounting of the piezo on the actuator membrane deserves special attention. Conductive epoxy glue (EPO-TEK H20S) was used in most cases. The electrical connections were made with the same glue.

When the backside of the membrane is metallized it is possible to use a non-conductive glue. With a high actuation frequency the glue layer will then act as a capacitor. As long as the capacitance of the glue layer is lower as that of the piezo actuator the losses will be low.

The main demand put out for the glue here is the electrical conductivity, and not so much the mechanical properties. The overall quality factor of the resonances should improve when a stiffer glue can be used.

3.5.3 The fluid-connection

The device needs some connection to a fluid reservoir. The simplest way is by providing a hole in the side of the device and gluing a syringe needle in this hole. The standard connection of the syringe needle can be used to connect up a host of equipment.

The placing of the syringe needle proved to be a critical step in the assembly procedure. Easily glue was taken in the hole to block the entrance. An improved fluid connection was made from PEEK[1] (see fig. 3.21). The assembly was easier

---

[1] Polyetheretherketone.

***Figure 3.21**: The two types of fluid connections. Left the syringe needle, right* the *PEEK connector.*

that way but the resonance behaviour of the device changed (see also the next chapters).

3.5.4 Alternatives

An interesting alternative to gluing of the device halves and also the mounting of the piezo, might be eutectic bonding. It is more critical to the surface conditions but less demanding as compared to anodic bonding. It is also much stiffer then the epoxy glue and has a higher chemical resistance. Si forms with Au an eutect with a melting point of 363°C. Other eutects of interest include Au-Sn (eutectic point at 280°C) and Au-In (eutectic point at 224°C).

3.6 Implementation

The principle design for the vaporiser is that of the face shooter as presented in fig. 3.13 and 3.20. The actual device was assembled from two parts, each one silicon wafer thick (400 μm thick in this case). The device was for the first series 15 x 15 mm^2 and later this was changed to 10 x 10 mm^2. The actuator membrane (the backside of the device) was etched 50μm thick at first, later this was changed to 200μm. The thicker membrane showed better characteristics for drop on demand (as will be explained in chapter 5). The nozzles were etched with DRIE through

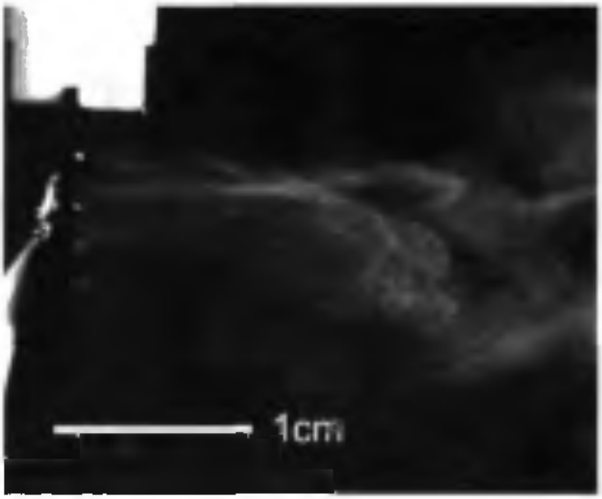

Figure 3.22: *The device during operation. The fluid connection is on the top side in this configuration.*

membranes of 10 to 20 μm thick. A timed etch-stop was used for both membrane thicknesses. The curvature of the original wafer cause some spread in the actual thickness of the nozzle membranes. The device can be seen during operation in fig. 3.22.

During the first phase of the development the main interest was to raise the number of nozzle on one device to see if sufficient throughput was possible. The first generation of devices had one nozzle etched by KOH. The second generation had one or several nozzles etched with the DRIE process (see fig. 3.23). The smallest nozzle then was $10\mu m$. Then in a number of parallel series, devices were fabricated with 60, 600, 1300 and 1800 nozzles. To arrive at such a high number of nozzles it is necessary to place more then one nozzle in each membrane, as shown in fig. 3.24. Through all these series the basic layout did not change.

In chapter 5 the optimisation of the basic design will be discussed. Here the layout will change to arrive at optimum device characteristics.

Figure 3.23: *Four nozzles of 10μm etched in one membrane.*

Figure 3.24: *Many nozzles etched in one membrane. Also visible the extra chamber as it is necessary for the designs of chapter 5* and *6*

3.7 Conclusion and Discussion

Many droplet ejection devices exist, but only a limited number have the potential of being used for IDT. Fig. 3.25 summarises the design choices made in this chapter. The basic layout and technologies are known now. The dynamic behaviour of the assembled device is the main interest of the next chapters. Once the dynamic behaviour is understood mass production can be investigated.

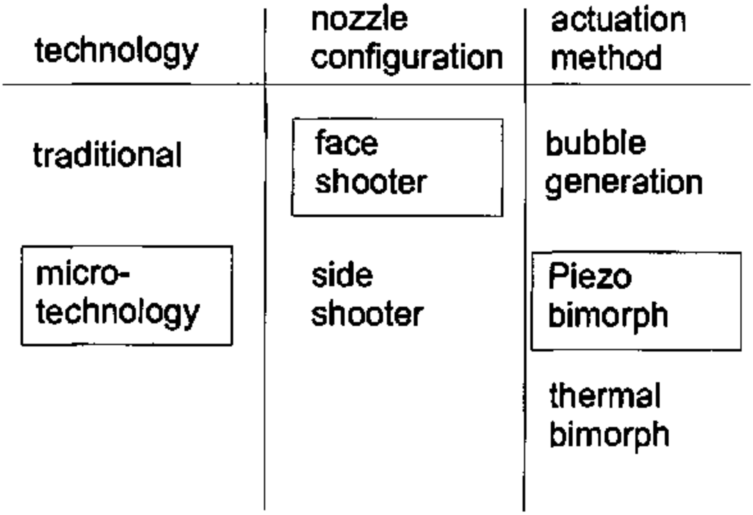

Figure 3.25: *The different possibilities to build a drop on demand device. The choices for the vaporiser to be used in the 'smart inhaler' are boxed.*

First tests showed that the chosen layout and technique have sufficient potential to comply with the demands set-out in the previous chapters. So far no fundamental limits were found for the droplet size, smaller nozzles produced smaller droplets. The first devices showed problems with leakage from nozzles that do not receive sufficient amplitude to eject droplets.

The high actuation frequency makes that the device no longer resonates in its first or fundamental mode but in one of its higher order modes. This means that certain parts of the surface move in anti-phase with other parts. But also nodal lines, i.e. lines that do not move at all, can be found. This complicates the layout possibilities. Chapters 4 and 5 will go into the analysis of these phenomena.

Bibliography

[3.1] Fan-Gang Tseng, Chang-Jin Kim, and Chih-Ming Ho. A novel microinjector with virtual chamber neck. In *proc. MEMS'98 Heidelberg*, pages 57–61, 1998.

[3.2] F.L. Switzer. A versatile system for stable generation of uniform droplets. *Rev. Sci. Instrum.*, 62(11):2765–2771, 1991.

[3.3] M. Kurosawa, T. Watanabe, and T. Higuchi. Surface acoustic wave atomizer with pumping effect. In *proceedings of MEMS'95, Amsterdam*, pages 25–30, 1995.

[3.4] M. Kurosawa, A. Futami, and T. Higuchi. Characteristics of liquids atomization using surface acoustic wave. In *proceedings of Transducers '97*, pages 801–804, 1997.

[3.5] Lord Reiyleigh. *Proc. Lond. Math. Soc.*, 10(4), 1878.

[3.6] D.B. Bogy and F.E. Talke. Experimental and theoretical study of wave propagation phenomena in drop-on-demand ink jet devices. *IBM J. Res. Develop.*, 28(3):314–321, 1984.

[3.7] P. Zanen. *Aerosol formulation and clinical efficacy of bronchodilators*. PhD thesis, Universiteit Utrecht, Faculteit geneeskunde, 1999.

[3.8] S.O. Shiryaeva and A.I. Grigor'ev. Mode analysis of drop detachment during electrohydrodynamic atomization of liquids. *Technical Physics*, 40(1):12–17, 1995.

[3.9] K. Tang and A. Gomez. Generation by electrospray of monodisperse water droplets for targeted drug delivery by inhalation. *J. Aerosol science*, 25(6):1237–1249, 1994.

[3.10] A. Zollner, B. Hochwind, and M. Fahndrich. Thermodynamic and fluid dynamic simulation of micromechanical manufactured bubble-jet printheads.

[3.11] S. Hirata, I. Yorishige, H. Matoba, and R. Inui. An ink-jet head using diaphragm microactuator. *IEEE*, pages 418–423, 1996.

[3.12] S. Kamisuki, T. Hagata, D. Tezuka, Y. Nose M. Fujii, and M. Atobe. A low power, small, electrostatically driven commerial inkjet head. In *Proceedings of MEMS '99, Heidelberg*, pages 63–68, 1999.

[3.13] J. Nilsson, T. Laurel, L. Wallman, and J. Drott. A flow-through liquid picoliter sampling cell. *Analytical Methods & Instrumentation*, Special issue μTas '96:88–90, 1996.

[3.14] Microdrop GmbH. Norderstedt, FRG, germany.

[3.15] W.G. Hawkins, C.J. Burke, T.E. Watrobski, T.A. Tellier, and S. Verdonckt-Vandebroek Adn T.P. Chow. A fully integrated silicon-based 40v thermal in jet ic. *Microelectronic Engineering*, 19:165–170, 1992.

[3.16] P. Lughinbuhl, P.-F. Intermuhle, M.A. Grétillat, F. Willemen, N.F. de Rooij, D. Gerber, G. Gervasio, J.-L. Vuilleumier, D. Twerenbold, M. Düggelin, and R. Guggenheim. Micromachined injector for DNA mass spectrometry. In *Proceedings of Transducers '99*, pages 1130–1133, 1999.

Chapter 4

Characterisation

Abstract

Two main characterisation interests can be distinguished; the vibration characteristics of the device and the ejected droplets. As analysis techniques for the vibration characteristics, impedance measurement and interferometry were used. It was found that operation is resonance dependent and that complicated mode patterns exist at these frequencies. For the characterisation of the droplets a stroboscope and high speed video camera were used. The size of the droplets was measured using Laser Doppler Anemometry. The measured size distribution showed that also for small nozzles the droplets are of the same size as the nozzle and that the achieved size of the droplets lies within the target range of 4 to 5 μm. The flow through the device was measured by measuring the weight loss of the device.

4.1 Introduction

In the characterisation two main goals can be distinguished. First: The characterisation of the device itself through impedance measurements and interferometry; Trying to understand its operational parameters. Second: Characterisation of the aerosol generated through high speed video and laser doppler anemometry, and checking this with the demands set out in the previous chapters (Chapter 2). In this the diameter and total throughput of droplets is measured.

Several techniques are necessary to come to a full characterisation of the device. These techniques will be introduced in this chapter.

Part of the characterisation runs in parallel with the modelling and optimisation; measurements were necessary to validate the model. On the other hand were measurements necessary to confirm the insight in the mode of operation of the device.

4.2 Measuring device behaviour

The drop on demand device as proposed at the end of chapter 3 operates at a frequency far beyond its first resonance frequency. This means the front and back side no longer vibrate in a regular fashion but patterns exist where different parts of the device move with a different phase and amplitude. The complexity depends on the actuation frequency; the higher the actuation frequency the more complex the pattern or *modeshape*. Knowledge of the modeshape can help place the nozzles in such a way that they all eject droplets. Nozzles that are not properly placed can start leaking and cause large droplets on the front plate that can impair functioning of the device.

The ejection of droplets depends on the combination of the movement of the front and back side. Picking out the right higher order resonances for operation guarantees a maximum amplitude and a predictable vibration behaviour. The electrical impedance can be measured on the connections of the piezo actuator, this gives information about the frequencies of the different resonances. Using optical methods the actual vibration of the frontside with the nozzles of the device can be visualised.

4.2.1 Impedance/phase measurement

Measuring the electrical impedance of the device gives information about the resonance behaviour of the device. The electrical impedance is normally measured in the ohmic resistance and the phase. These are defined as;

$$\begin{aligned} Impedance &= \frac{|U|}{|I|} \\ Phase &= \arccos(\overline{U} \cdot \overline{I}) \end{aligned} \tag{4.1}$$

These values are measured as function of the actuation frequency in the form of an impedance curve. The curve shows a minimum in the impedance and a bending point in the phase where there is a resonance .

Apart from predicting where a device has its resonances and where it might function, it also gives information about the stability of its functioning and the power consumption. Important to notice is that this measurement does not tell us in which exact mode a device resonates, i.e. the pattern of vibration is not shown. So is it very well possible that a certain peak does not correspond to a vaporising mode.

Experimental

For impedance/phase measurement an HP 4194A was used. Measurement data was transferred to a PC though HP-IB and treated with Excel. In a characteristic chart both the resistance and phase are plotted against the frequency.

Results

The piezo acts as a capacity, thus the basic impedance falls off with $1/f$ and the phase is fixed at -90°. All mechanical vibration behaviour shows up as a superposition on this basic curve. Fig. 4.1 is the impedance curve of a typical device around its first resonance frequency. The phase in not completely at -90°, due to some series resistance in the piezo itself and between the electrical connection of the piezo. This curve shows two resonances and two anti-resonances. At an anti-resonance there is no movement at all and the impedance has a (local-) maximum. Apart from the frequency of a certain resonance also the quality factor of that resonance can be seen. The quality factor is the ratio between the width of the

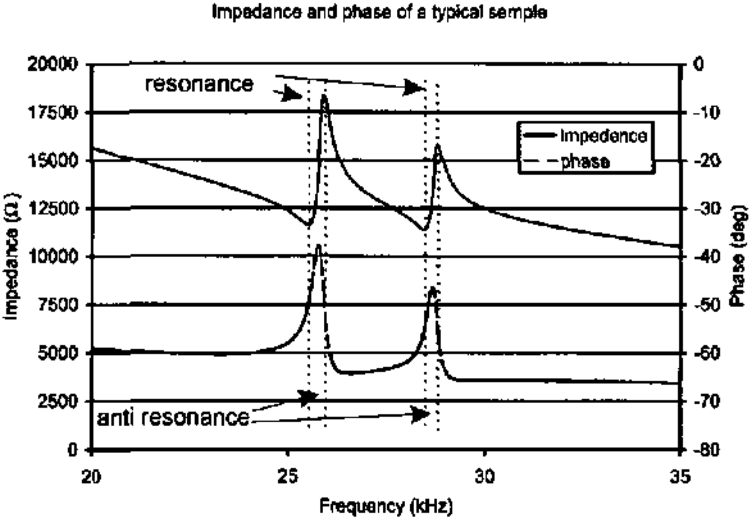

***Figure 4.1**: Impedance/phase diagram of a typical device. The region where the first resonances appear is shown.*

resonance peak halfway down from the top (full width at half maximum) and the resonance frequency.

The quality factor gives information about the power consumption of the device when it is in resonance. The higher the quality factor the less energy its needs to sustain its amplitude. An important concept is connected with the quality factor; mode-mixing. One resonance peak that appears close to an other can 'leak' energy to the other resonance. The resulting mechanical movement is a combination of the two separate modes. This concept will be further explained in the theory part of chapter 5. The higher the quality factor the less problems with mode-mixing occur.

The basic 10x10 mm^2 device has a first resonance around 30kHz, for smaller nozzles this frequency is not of interest, due to the low throughput. The most interesting area lies in the 200 to 300kHz range.

Fig. 4.2 shows a larger portion of the spectrum of a device of a later generation then fig. 4.1. Again isolated resonances can be seen, for instance in the 100 to

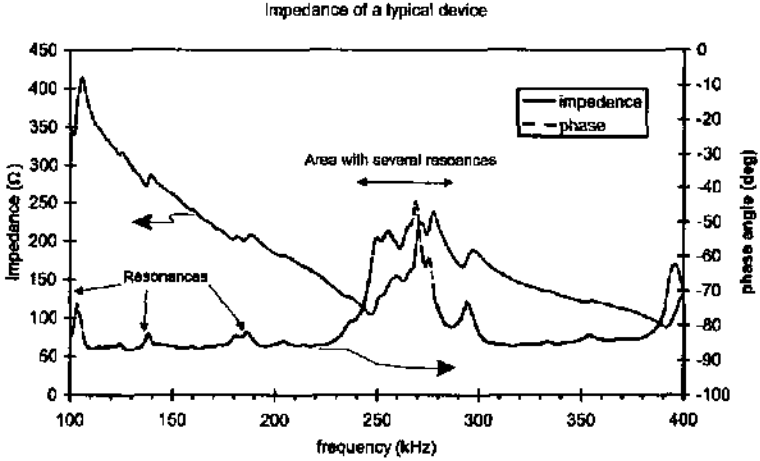

Figure 4.2: Typical impedance/phase diagram.

200kHz range. A second region, between 230 and 290kHz, can be identified where there are many peaks appearing together. In this area the quality factor was too low to keep the peaks separated from each other. For this device several frequencies where droplet ejection is possible appear in this 230 to 290kHz window. It is very difficult to distinguish which exact peak correspond to the resonance that causes droplets to be ejected.

Using a 'noisy' actuation signal in an area with many peaks will activate a number of modes and consequently give an apparent stable ejection pattern (this effect is connected with the explanation of the forced vibrations in par 5.2.1). This behaviour was observed when using an actuation signal with considerable noise (estimated from the oscilloscope measurement a bandwidth of some 10kHz). Disadvantage of this mode of operation is that the behaviour is as unpredictable as the noise in the generator, not all nozzle are functioning all the time and so it becomes difficult to predict the flow. Also the nozzles that are, temporarily, non-ejecting can start leaking.

The measurements shown in fig's 4.1 and 4.2 were done on an empty devices, i.e. there was no water in the fluid chamber. The water in the chamber could

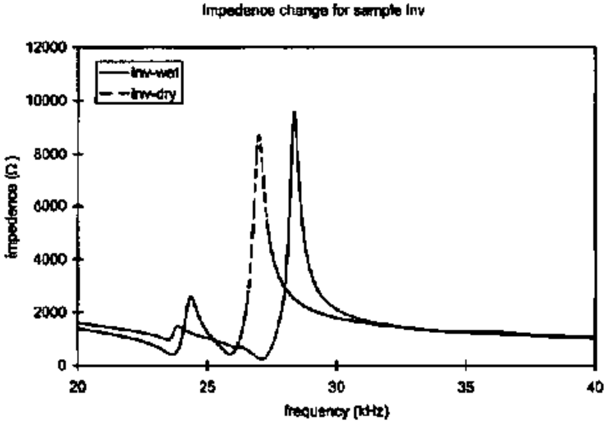

***Figure 4.3**: Typical measurement result, for a empty (dry) and filled (wet) device.*

influence the vibration behaviour; there would be an extra coupling between the back and front side and there is extra mass in the system. This problem is also of importance for the modelling. When there is little difference between the filled and empty device a model of only the mechanical part will be sufficient and a large amount of calculation time can be saved.

The impedance measurement was the only way to confirm that there is little difference between a device that is filled with water and one that is empty. The only influence that could be observed in the impedance curves is that the resonances move in frequency when the device is filled (c.f. Fig. 4.3 and 4.4). During the filling of the device the different peaks could be seen moving from the dry to the wet position. Some resonance peaks got weaker due to some damping, others got stronger. Most important, non of the peaks crossed with an other, which means the oscillation behaviour did not change fundamentally. This means that there is so little influence from the liquid in the device that it is valid to do measurements and simulations on empty devices and so do predictions for the behaviour of filled devices.

Several different fluid connections were used. Some devices functioned better with one type of connector then with others. The influence of different types and

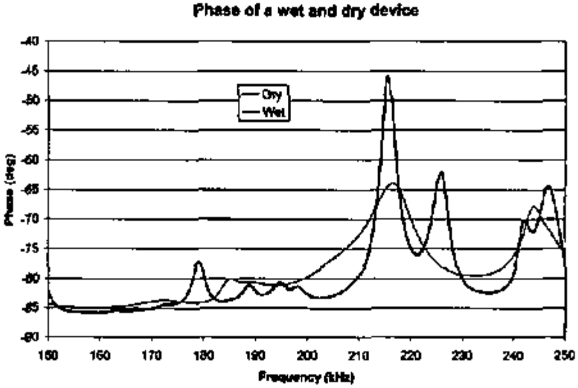

Figure 4.4: *Typical measurement result in the high frequency range, for an empty (dry) and filled (wet) device. Some modes almost disappeared others moved slightly in frequency.*

places of the fluid connection on the resonance peaks could clearly be seen (see fig 4.5). This is connected with the different movement of the sides with the different modes. This means that there is an influence from the fluid connection and that special care should be taken when trying to model this behaviour.

4.2.2 Interferometer

Not all resonances correspond to frequencies where the device ejects an aerosol and not all frequencies work equally well. This can be explained with the different modeshapes and differences between the movement of the front and backside. To gain insight in this problem, observations of the actual modeshape are necessary.

To observe the movement of the front surface of the device a interferometer in combination with a high speed video camera was used. This set-up gives direct information about the actual shape of the resonance mode and about the stability of these modes. The mixing of neighbouring modes can also be observed.

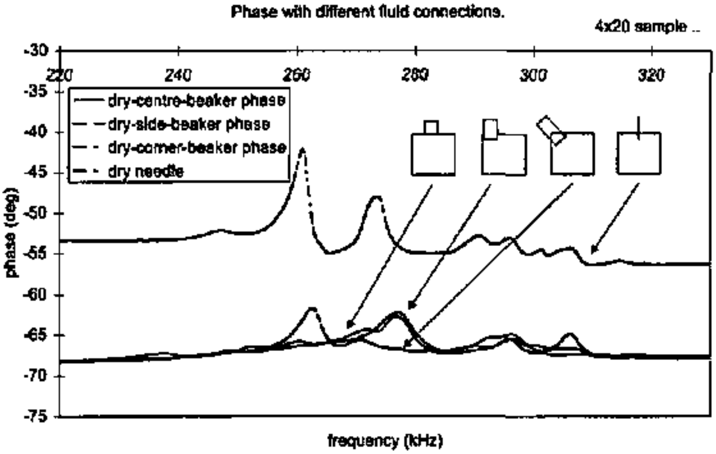

***Figure 4.5**: The influence of the fluid connection on the different resonances. The needle connection was measured on a different sample, which explains the off-set. Only the phase curve is shown for clarity, off course the impedance curve changed as well.*

Experimental

The set-up is a basic Michealson interferometer [4.1] (see Fig.4.6) with the frontside (with the nozzles) of the device as measurement mirror in one leg and the high speed camera at the receiving end. The source consists of a HeNe-laser ($\lambda = 632.8\ nm$) and a beam broadening set of optics. The beam broadener consists of a 40x microscope objective, a pinhole of $10\mu m$ diameter and a lens with 80mm focal length. First the laser beam is focused on the pinhole. This forms a high luminescent point source. Placing this in the focal point of the lens forms a uniform and parallel beam.

The beam is split up in two coherent beams by the beam splitter. One part reflects of the front surface of the device and the other of a reference mirror. The reference mirror is of the same material as the device to get an equal reflectivity and so equal intensity.

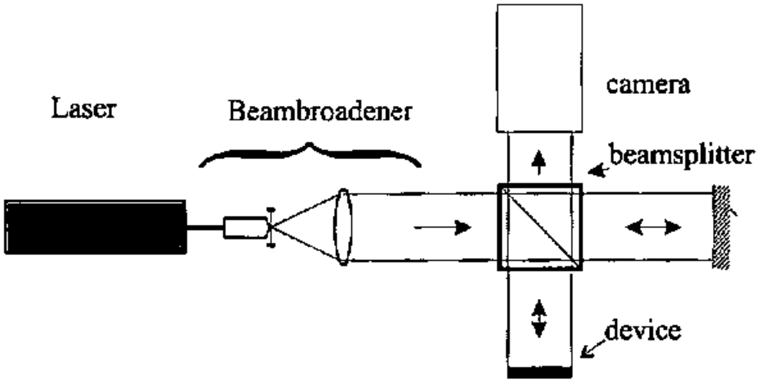

Figure 4.6: Layout of the interferometer set-up

On the CCD the two parts of the beam meet again. If the distance travelled by the two parts is such that the light waves are in phase, they will produce a light spot. If they are in opposite phase they will extinct and form a dark spot. Opposite phase corresponds to a $\lambda/4$ length difference between the two legs of the interferometer.

Using an exposure time that is longer then the actuation period of the piezo shows the moving parts as gray area's. The front surface will move and so the length difference between the two legs changes, resulting in a series of light and dark spots. The nodal lines of the mode pattern do not move and show the basic interference pattern.

It was not possible to observe the front surface with the nozzles while the device generated an aerosol because the aerosol obstructed the optical path.

The backside of the piezo on device was not accessible for measurement either. The nickel surface of the was too diffuse. Any action to improve the reflectivity would change the mechanical properties and thus the device's behaviour.

Results

The combination of interferometer and impedance measurement gave information about the movement of the device during actuation. Fig. 4.7[1] shows the combination of a number of interferogrammes and a phase curve. The three resonances shown clearly correspond with the bending points in the phase and thus the minima in the impedance.

It is not straightforward to measure the amplitude of the vibration. In theory is the movement of one interference fringe (one light-dark-light series as seen by a pixel on the screen) is equal to $\lambda/4$ movement of the measurement mirror in the beam direction. The stability of the set-up did not allow for such detailed observation.

Still it is possible to give an indication of the amplitude. This can be done by realising that when the amplitude is exactly $\lambda/4$ the rings smear equally gray. That means that a point in the image sees a equal amount of dark and light. If the amplitude gets higher some area's are longer in the dark then others. Looking for these points in the pictures tells something about the amplitude (see also fig. 4.8).

Figure 4.9: *Interferogrammes of a device vibrating at 115.6kHz, taken with different amplitudes. The image is taken over the full front surface (10x10* mm^2*)*

0.65V

---

[1] Again from this phase curve is clearly visible the shift between the empty device (WET) and the filled device (DRY). The change in quality factor between the empty and filled device makes some peaks almost disappear.

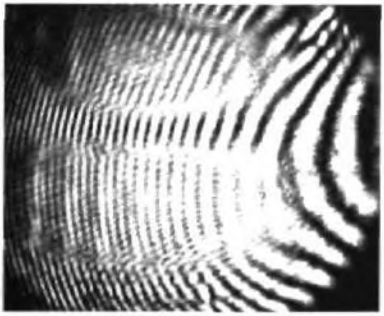

1.26V

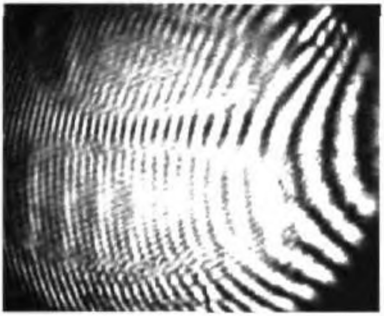

1.44V

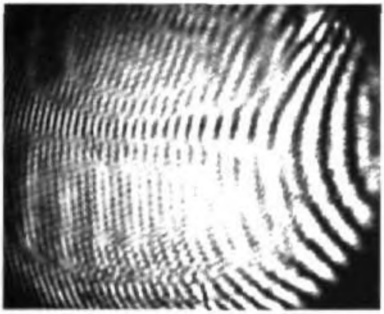

1.96V

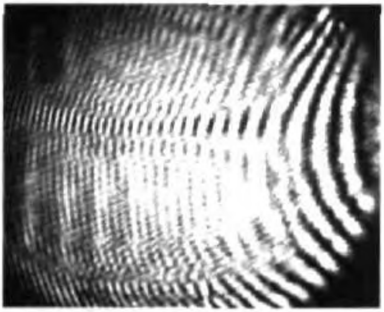

2.22V

Fig. 4.9 shows a series of interferogrammes with increasing actuation amplitude. The first one taken at 0.65V amplitude shows gray area's where there is movement, and the area's where the original interference pattern still exists (the nodal lines). This particular mode is the (2,1) mode, where two area's are moving. It can be seen that with growing amplitude the moving part gets larger. The last in the series (at 2.22V) shows in the top halves two bands parallel to the extreme of the moving area where the basic interference pattern seems to appear again. At these places the amplitude is such that one interference fringe moves exactly halve a fringe. During the exposure time the area between two original fringes is now longer in the dark and thus a dark band appears. The maximum amplitude of this part of the device can now be deduced. The amplitude is between $\frac{1}{4}\lambda$ and $\frac{3}{8}\lambda$. With the wavelength of the HeNe laser this gives an amplitude of 150 to 200nm for this actuation amplitude.

4.3 Measuring Droplets

The size of the ejected droplets not only depends on the size of the nozzle but also partly on the actuation amplitude and frequency [4.2]. To investigate this it is necessary to observe the droplets during and after ejection. When the ejection is very regular a stroboscope can be used. The set-up consists of a standard video camera and an LED (HP, HLMP3750) in contrast mode, as light source. With a standard 30fps camera images are taken every 33ms. For an actuation frequency of 100 kHz this means that an image is built up of 3300 overlying exposures. The actual image is now the envelop of all separate actuations. For ejection regimes that are less regular it becomes necessary to look at individual actuations. This is possible using a high-speed video camera (Sensicam with an Intravision long distance microscope, from PCO: www.pco.de).

With many nozzles in parallel it gets more difficult to look at individual droplets. Also a more representative measurement is necessary. Laser Doppler Anemometry (LDA) measures many droplets and thus give the statistical distribution of the

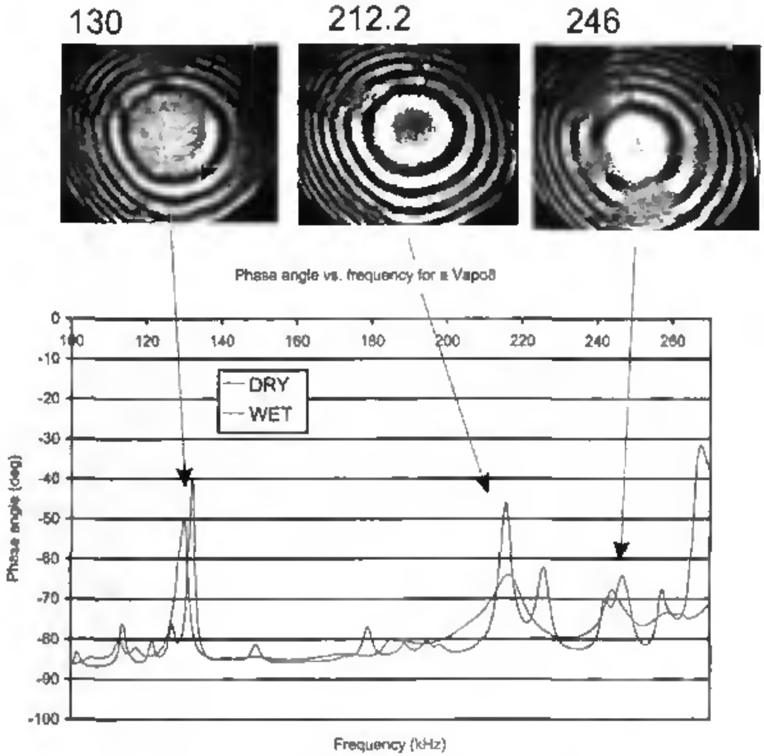

***Figure 4.7**: Comparison of the interferometer output and phase curve. The left interferogramme is added from a different measurement but shows a basic interference pattern when there is no actuator signal. The rings will smear out under the movement of the front plate.*

droplet sizes [4.3, 4.4]. An LDA system consists of two coherent laser beams that cross under a sharp angle, at the measurement point. The measurement signal is the frequency shift between the reflected beam and the original beam (Doppler effect). By using two detectors under different angles and measuring the phase between the two measured signals, the size of the observed droplet can be deduced.

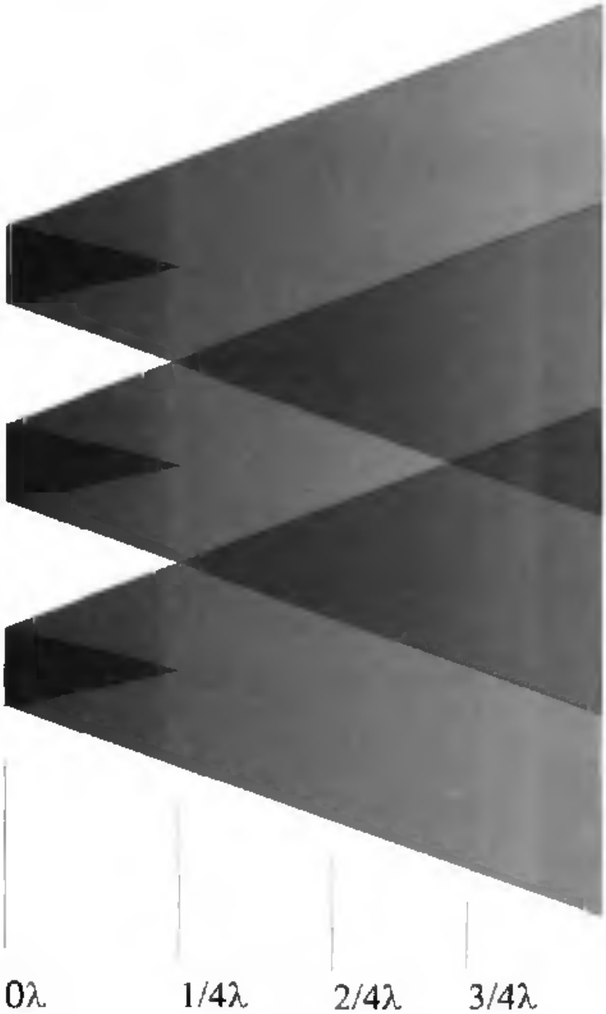

Figure 4.8: *Measuring the amplitude with the interferometer. At the left side of the picture there is no movement and the interference fringes are sharp. With rising amplitude the rings smear out until they touch ($\frac{1}{4}\lambda$). At even higher amplitude there are area's that see more dark then light and appear again as fringes.*

***Figure 4.10**: 70 μm nozzle shooting 65 μm droplets, actuation frequency is 45kHz. Due to the stroboscopic effect, the picture consists of 1500 overlying exposures.*

4.3.1 Stroboscope

The first devices that were made in our laboratory had square nozzles of $70\mu m$. To analyse the ejection behaviour of these devices we used a stroboscope. The set-up consisted of a simple video camera and an LED (HP, HLMP3750) as light source. With a standard 30fps CCD camera images are taken every 33ms. For an actuation frequency of 100kHz this means that an image is build up of 3300 overlying exposures. The droplet ejection could be followed in detail by using a strobe frequency that was slightly different from the actuation frequency. The speed of the droplets could be deduced from the distance between them multiplied by the actuation frequency, provided that only one droplet was ejected per actuation. The smearing on the right is due to the noise in the synchronisation of the stroboscope and the droplet ejection. The finite flash length shows up as an extra smearing in the movement direction of the droplet. Shorter light pulses would have been possible with a gas discharge lamp.

From the bigger nozzles (20 μm and up) the observed droplets are ejected in a very regular manner. It is possible to us as stroboscope to observe and measure the droplets. Fig. 4.10 shows a typical result, here a 70 μm nozzle is working in the drop on demand mode at 45 kHz. The droplets have a diameter of 65 μm. The speed of the droplets can be deduced from the distance between them multiplied by the actuation frequency, provided that only one droplets gets ejected with every actuation. The speed in Fig. 4.10 is $14\,{}^{m}/_{s}$. At higher frequencies and with smaller droplets a stroboscope is less suitable as the droplets start behaving too much in a random manner. Droplets down to $10\mu m$ and actuation frequencies of 120kHz were the limits of the stroboscopic system. The measurement accuracy for droplet diameters is $\pm\ 4\mu m$. Distances between droplets could be measured with $\pm\ 10\mu m$ accuracy.

4.3.2 High-speed Video

With the high-speed camera it is possible to observe single droplets. The problem here is to have enough light to get a well-exposed picture. The best results were obtained in contrast mode, where a high power halogen lamp was placed directly opposite the camera. Figs. 4.11, 4.12 and 4.13 show the droplets ejected from a $20\mu m$ nozzle with rising actuation amplitude. The actuation pulse causes liquid to be pushed out of the nozzle. The surface tension of the liquid tries to minimize the surface of the liquid outside the nozzle and so causes a restoring force pushing the liquid back in. In a dynamic situation, the kinetic energy of the liquid outside the nozzle causes the droplet to deform length wise. When the kinetic energy is high enough the liquid can break through the surface tension and so form a free droplet. At the lower amplitude limit droplets will from in a regular manner (Fig. 4.11). The higher the amplitude, the more the droplet will deform before break off. At a certain amplitude the 'tail' of the droplet can break off the main droplet and form a so called satellite (fig. 4.12). At even higher amplitudes, the kinetic energy gets so high that the surface tension is no longer able the hold the droplet together. In this case the ejected droplet will break up in several smaller droplets (Fig. 4.13).

These regimes cause characteristic size distributions. The regular regime will only generate droplets of one size. At higher amplitude the generated satellites are of a smaller size and so cause a spread in size. The chaotic regime gives a lower average droplet size as compared to the others but also less control of the actual droplet size. For inhalation applications the first, regular, regime is preferable.

The optics limit the measurement accuracy to $\pm 1\mu m$. The shutter time of the camera was typically $2\mu s$. With this there were less problems with smearing of

***Figure 4.11**: High-speed video image of regular droplet ejection.*

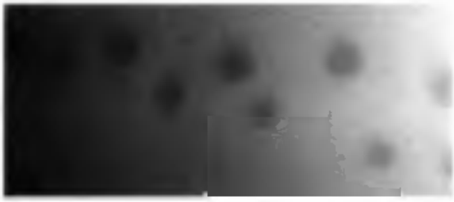

***Figure 4.12**: High-speed video image of satellites, due to a too high actuation amplitude.*

***Figure 4.13**: Chaotic droplet ejection. The nozzle is situated on the left and ejects an elongated droplet that beaks up in several smaller droplets later on. The scale is half that of the other two pictures*

the image in the movement direction.

Droplets from closely spaced nozzles were observed to merge with one another after they were ejected. Fig. 4.14 shows a quasi time loop of this behaviour. Droplets on the left were ejected more recently than the ones more to the right. From this kind of observation it was concluded that a minimum spacing of $25\mu m$ was required for optimal droplet generation. These measurements were performed

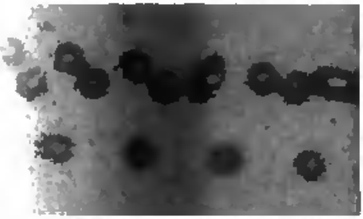

***Figure 4.14**: Merging droplets of 10μm. The nozzles are located on the left.*

on a standard device before the optimisation (chapter 5) and are therefor done for only one frequency and the maximum amplitude of the oscillator ($10V_{pp}$). It will be interesting to re-do this measurement with the optimised device so that there is a clear relation between the actuation amplitude and the pressure pulse at the nozzle.

4.3.3 Laser-Doppler anemometry

The next devices that were developed contained several 100 even smaller nozzles in parallel, making it very difficult to observe single jets. The method to measure the droplet size in this case is LDA. With LDA the size of a large number of droplets can be measured in a short time period, but no direct information about satellites or chaotic break-up is available. It is therefor harder to interpret the measurement results. Fig. 4.15 shows a typical size distribution for a device working at a frequency between 250 and 300kHz, having 600 $5\mu m$ diameter nozzles. Actuation was done with a $20V_{pp}$ signal. There are two ways to calculate the average 'size' of the droplets. The first accounts only the diameter and is therefor the size average. The second calculates the diameter of the average mass of the particles and is therefore the mass-average diameter. For this measurement the size average diameter is $4.5\mu m$ and the mass-average diameter is $5.0\mu m$, which lies in the desired size-range for administration of medicine. The measured speed is about $1\ ^m/_s$, which is perfect for medicine delivery (the flow speed for inhalation is around $2\ ^m/_s$). The LDA system has a measurement accuracy of $\pm 20nm$ for the

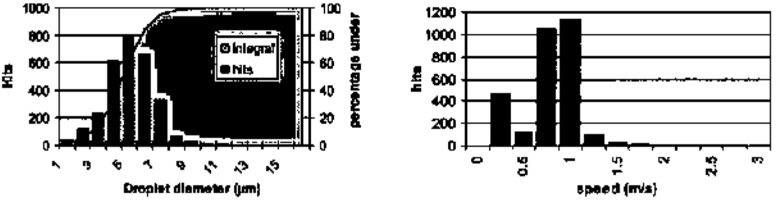

***Figure 4.15**: The laser doppler measurement of a device with 5 µm diameter nozzles, working at a frequency of 250kHz. Left the size of the droplets, right the speed of the same droplets. The diameter-average size is 4.7 µm and the mass-average size, 5.0 µm.*

diameter, assumed that the droplets are round.

The distribution in size can be caused by a combination of the effects shown before, for the bigger nozzles (fig's 4.11-4.13). This because not every nozzle sees the same actuation amplitude; the ones closer to the antinodes of the resonance modes see a higher amplitude then the ones closer to a nodal line.

4.4 Flow measurement

An important characteristic of the device is the total flow of medicine and the flow stability; patients need to get the same medicine dose every shot. To measure flow directly one can use a flow sensor in the supply line of the vaporiser or a more indirect method can be used by weighing the device before and after a shot.

Most direct flow-sensors use a pressure drop to measure the flow. This pressure drop influences the functioning of the device. Furthermore is the pressure drop a function of the flow so the system gets very dynamic and very complicated. The flow sensor measurements were used for indicative purposes only.

4.4.1 Weight measurement

More accurate then the flow sensor, and less disturbing for the system is weight loss measurement. Here the supply beaker is placed on a balance, and one can

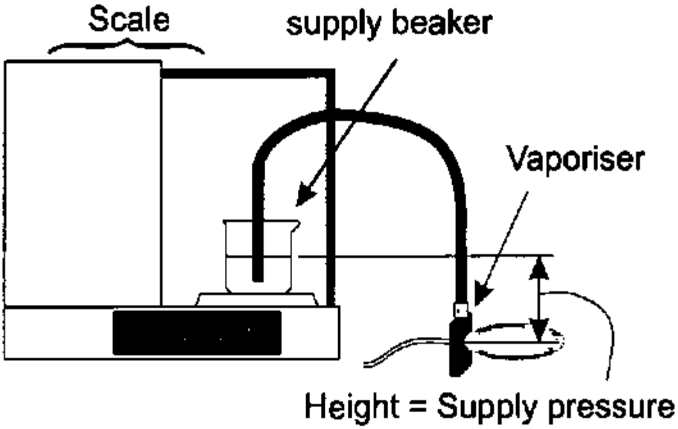

***Figure 4.16**: The weight measurement set-up. The supply pressure is given by the hight difference between the supply beaker and the vaporiser.*

measure the flow by looking at the weight loss of the beaker after a certain time. The experimental setup is shown in fig. 4.16. The scale measures with $0.1\mu g$ accuracy which means the total flow can be measured up to $0.1\mu L$ accuracy. The actuation was done in a shot to shot fashion, i.e. the vaporiser was actuated for a certain period and then the total flow out of the device was measured. The time period was defined using a second function generator, with an uncertainty in time definition far superior to that of the weight measurement.

The effective number of nozzles working can be calculated from the actuation frequency and the volume of a single droplet.

A typical flow measurement compared with the phase angle from the impedance measurement can be seen in fig. 4.17. There is a considerable spread in the data points, the cause of this will be investigated in chapter 6. Despite the spread in data it can still be seen that the maximum flow occurs where there is a maximum phase change and thus the peak of the resonance.

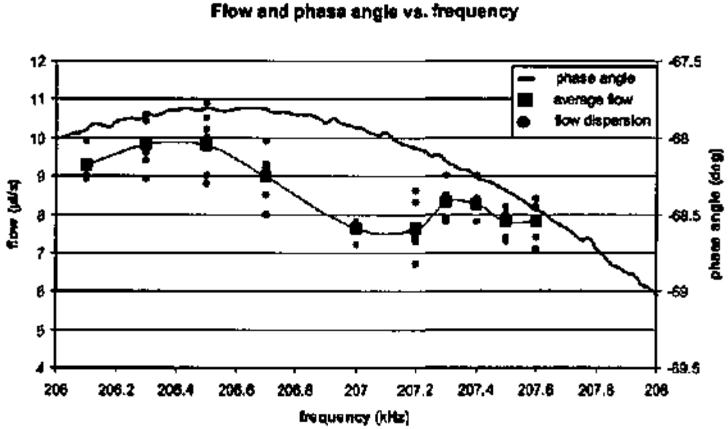

Figure 4.17: Typical flow measurement using the scale, compared with the phase angle of the impedance measurement. This measurement will be further discussed in chapter 6.

4.5 Conclusion and discussion

Different characterisation techniques were used to get insight in the functioning of the vaporiser. Impedance measurement and interferometer observations showed the resonance behaviour. The next chapter will use these results to start an optimisation procedure.

The behaviour of the droplets was observed using a high-speed video camera. Different droplet ejection regimes were found as function of the actuation amplitude. Measurements on devices with many nozzles working in parallel showed distribution of sizes narrow enough to comply with the demands set out in chapter 2. The observed distribution is due to differences in actuation amplitude over the device's front surface. Also merging of droplets could cause part of the distribution.

The total flow shows some instabilities, but still a clear connection with the resonances could be seen. This is also an indication that resonances are an important aspect of the operation of the device.

Bibliography

[4.1] E. Hecht. *Optics, second edition*. Addison Wesley Publishing Company, 1987.

[4.2] F.L. Switzer. A versatile system for stable generation of uniform droplets. *Rev. Sci. Instrum.*, 62(11):2765–2771, 1991.

[4.3] W.D. Bachalo. Method for measuring the size and velocity of spheres by dual-beam light-scattering interferometry. *Applied Optics*, 19(3):363–370, 1980.

[4.4] M. Saffman, P. Buchhave, and H. Tanger. Simultaneous measurement of size, concentration and velocity of spherical particles by a laser doppler method. *Laser Anemometry in Fluid Mechanics II*, pages 85–103, 1984.

Chapter 5

Modelling and optimisation

Abstract

An FEM model of the vaporiser was constructed to analyse the vibration behaviour of the device. The first simulation models were made for existing devices to validate the simulation platform. With these results, optimisation criteria and optimisation parameters were identified. Three different device designs were optimised, each for a particular vibration mode. Two of these designs showed sufficient stability to be used as vaporisers.

5.1 Introduction

It was already seen in chapter 4 that the operation of the device is connected with the presence of resonance modes. Interferometer observations and impedance measurements confirmed this as demonstrated in the previous chapter. The functioning of the device is not yet ideal, only certain parts of the front plate eject droplets and others parts do not function at all. Some parts in between do not seem to receive sufficient amplitude and form large droplets on the front plate that can eventually impair the functioning of other nozzles.

The measurements could not be used to measure the movement on the backside because there was not enough light reflected from this side. Any effort to improve the reflectivity would influence the mechanical properties.

To get more insight in the actual vibration and to look at the influence of the different device geometries a computer model was built. The goal of the simulation was to find the combination of movement on the front and back side and to optimise this movement for a certain resonance frequency.

The device as presented in chapter 3, consists of a silicon front and back side. The front side holds the membranes with the nozzles and the backside the piezo actuator. The device is connected to its fluid reservoir by a modified injection needle or a PEEK part. On the back side there are two electrical connections.

Before starting any modelling effort it is important to realise what has to be included in the model. It is unrealistic to put the whole device in a model, not only because of limitations in computer resources but also the number of unknown factors that might influence the device's behaviour. The goal of the simulation must be well defined, only then can an efficient and adequate model be built.

First of all the model domain has to be identified; what is part of the model and what is to interact with the model through boundary conditions. So the model only incorporated the silicon parts and the piezo. The results of this model will be compared with real samples to see if there is agreement or if the model needs extension with for instance the water in the chamber.

The vibration behaviour of the device is of interest; the functioning of the device is connected with the resonances of the device (see also chapter 4). This can be analysed with a calculation method called 'modeshape analysis'. Paragraph 5.2.1 will go deeper into modeshapes, resonances and how these can be calculated and influenced.

Once it is possible to model the behaviour of the device, the model can be used to do optimisation. Geometry variations can be tried without having to spend weeks in the cleanroom for fabrication. To do an optimisation, criteria have to be formulated as well as the parameters on which they are depending. Paragraph 5.4 goes into identifying the criteria and parameters and will show the optimisation results. Three optimised designs will be presented each with special characteristics.

5.2 Theory

5.2.1 Modeshapes, Resonances and Eigenfunctions

This paragraph will explain the modeshapes and resonances as they can be found in the device. This insight will help choosing the different optimisation parameters. First of all it is important to understand what a modeshape is and how it is connected with resonances. The best start is to look at a tight string, for instance a guitar string. It can be brought in a vibration by pulling it out of its equilibrium position and then releasing it. The frequency of this vibration is called the eigenfrequency or ground-tone of the string. The frequency depends on the tension in the string and its mass. When the string is displaced at $\frac{1}{4}$ and $\frac{3}{4}$ of its length in opposite directions, the resulting vibration will have a different pattern and frequency (see fig. 5.1). This is the *second* eigenmode and the frequency the *second* eigenfrequency. The displacement of the string is a particular pattern connected with the eigenfrequency, this pattern is called the eigenmode or modeshape. For the string a whole series of these modeshapes exist with increasing complexity and frequency. Mathematically these can be expressed as $sine$ functions. For a string the equation of motion can be written in $u(x,t)$, as [5.1]:

$$\begin{aligned} u_{tt} - c^2 &= u_{xx} \\ 0 < x &< l, t > 0 \\ u(x) &= 0 \ \text{ for } \ x = 0, l \text{ and } t > 0 \\ \text{with} : c &= \sqrt{T/\rho} \end{aligned} \tag{5.1}$$

With T the tension in the string and ρ it specific mass. The subscripts imply derivatives, double subscripts imply the second derivative. The modeshapes are the eigenfunctions of the mathematical system, the resonance frequencies are the eigenvalues.

The movement of the string is depending on its mass and tension as we saw above. For a prismatic beam the principal deformation is due to bending. Consequently the movement equation for a beam with a constant cross section changes

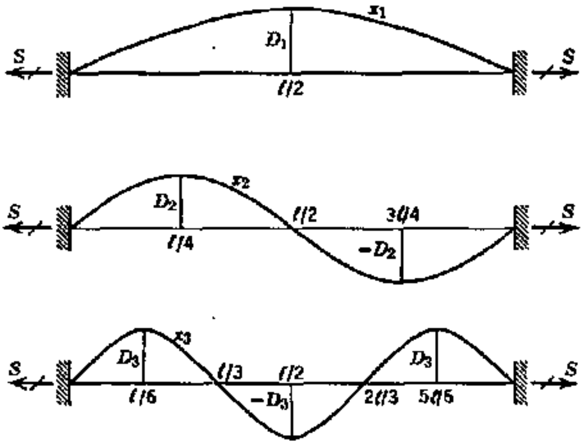

***Figure 5.1**: The first three eigenmodes of a string.*

to:

$$
\begin{aligned}
\frac{\partial^4 u}{\partial x^4} &= -\frac{1}{a^2}\frac{\partial^2 u}{\partial t^2} \\
\text{with } a &= \sqrt{\frac{EI}{\rho A}} \\
E &= \text{Young's modulus} \\
I &= \text{area moment of inertia} \\
A &= \text{cross sectional area of the beam}
\end{aligned}
\qquad (5.2)
$$

The movement of the beam is expressed in terms of the bending, this means that the solution of this equation is depending not only on the position of the ends of the beam but also on the rotation of the ends. If the beam is allowed to rotate around its ends but the position is otherwise fixed we get a set of solutions which is similar to the solutions for the string problem. This kind of boundary condition is called *simply supported*. If the ends are fixed such that no rotation is possible the boundary condition is called *fixed*. In general these kind of systems are solved by realising that a harmonic solution is of the form:

$$u(x,t) = \cos\omega t\{C_1 \sin kx + C_2 \cos kx + C_3 \sinh kx + C_4 \cosh kx\} \quad (5.3)$$

which gives a series solution in k.

A sting or beam that is forced to vibrate in a certain frequency will vibrate in exactly the same modeshape as the free vibration when the excitation force is applied with the right frequency. Forced vibrations with frequencies between two resonances vibrate in a modeshape that is a sum of the surrounding modeshapes. The further away the resonance frequency of a mode, the less it will contribute to the vibration behaviour. The underlying mathematical principles can be found in the theory of Fourier series [5.1].

A guitar string or a rod have only one degree of freedom (the $u(x,t)$) thus only one series of modeshapes exists. The complexity of the modeshapes rises with a rising number of degrees of freedom. A plate has modeshapes that are the superposition of two thin rod solutions, one in the x and the other in the y direction. The u is thus a function of (x,y) and t. The solutions of the vibrating plate problem are systematically given by Barton [5.2, 5.3], the frequency of a resonance can be expressed as:

$$\begin{aligned}
f_n &= \lambda_n \cdot \frac{\pi}{2a^2} \cdot \sqrt{\frac{D}{\rho'}} \\
D &= \frac{Eh^3}{12(1-\nu^2)} \\
f_n &= \text{frequency for a certain mode n} \\
\lambda_n &= \text{constant depending on the boundary conditions [5.2]} \\
E &= \text{Young's module} \\
\nu &= \text{Poison's ratio} \\
\rho' &= \text{weight per unit area} \\
h &= \text{thickness} \\
a &= \text{width}
\end{aligned} \quad (5.4)$$

Looking at the possibilities to influence the frequency at which a certain mode appears, several things can be noted:

- The λ_n are only depending on the boundary conditions.
- The actual mode frequencies can only be influenced by the material parameters.
- From these it is the thickness that the largest influence (it is taken to the 3rd power).

5.2.2 The FEM method

The problem gets more complicated if the beam or plate has a non-constant cross section. The I, the area moment of inertia; more or less how the mass is distributed over space, changes with the position and it will have to be taken inside the derivative. One way around these complications is the use of the finite element method (FEM). Here the problem is broken up in a series of partial problems. All these problems are put together to form a matrix equation. It goes too far to fully show the transformation of a continuous problem to a matrix problem, a treatment can be found in references [5.4]. The result of the transformation, is a equation of motion in $\ddot{u}$ and u [5.5]:

$$[M]\{\ddot{u}\} + [K]\{u\} = \{0\} \tag{5.5}$$

The matrix $[M]$ holds the (distribution of) mass of the structure and is comparable with the ρA term in 5.2. The $[K]$ matrix hold the stiffness information, comparable with the EI in 5.2. The continuous deflection function u is replaced by a displacement vector $\{u\}$ which holds the displacements of the discretisation points.

For a linear system, free vibrations will be of the form:

$$\begin{aligned} \{u\} &= \{\phi\}_i \cos\omega_i t \\ \text{where}\quad \{\phi\}_i &= \text{eigenvector representing the modeshape} \\ &\qquad \text{of the ith resonance frequency} \\ \omega_i &= \text{ith resonance circular frequency} \end{aligned} \tag{5.6}$$

Putting this in 5.5 gives the equation of motion for the harmonic case as:

$$\left(-\omega^2[M] + [K]\right)\{\phi\}_i = \{0\} \tag{5.7}$$

This is an eigenvalue problem that can be solved for ω_i and $\{\phi\}_i$. The ω_i are now the resonance frequencies and the $\{\phi\}_i$ the corresponding modeshapes.

The vaporiser can be seen as two vibrating plates that are tightly coupled through the rim. The two plates have different properties so that the vibration behaviour is not forcedly similar on the front and back side. The possible modeshapes are a combination of the front and backside and thus more complex than for a simple plate. The impedance measurements showed that the vibration is very stable so that it can be concluded that there is a very tight coupling in the rim. If this was not the case certain free vibrations could exist that show up as a beating signal in the impedance. The front plate does not have the possibility of its own free vibrations and is thus part of the whole vibration system.

5.3 Experimental

The system of eq. 5.7 gives the resonance frequencies and modeshapes of any structure. There exist computer programmes that build the matrices $[K]$ and $[M]$ from a given geometry and materials properties and which can solve the eigenvalue equation. The one used for this research is ANSYS 5.4. The smaller the partial problems in which the main structure is divided (the *elements* or *meshing*) the more terms there will be in the two matrices and the longer the computer will use to construct and solve the problem. A trade off is necessary between accuracy and available computer resources. After constructing the two matrices the computer scans through a pre-set frequency range and list all the eigenvalues found in that range.

5.3.1 Building the FEM model

It was decided to model only the two silicon parts and the piezo and to leave the other parts (fluid connection, electrical connections, water in the fluid chamber)

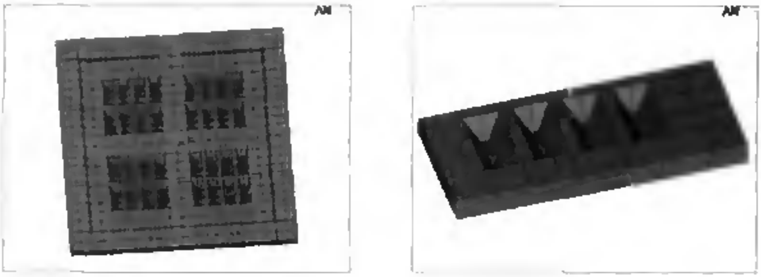

Figure 5.2: *The meshing of one side of the device and a detail of the membranes.*

out of the model. The membranes that hold the nozzles are so thin that they add only little to the stiffness. The nozzles will have even less influence. Therefore the front membranes are modelled with very few elements. Fig. 5.2 shows part of the meshed device. The fluid connection needs special attention. From the impedance measurements (see page 68) it could already be seen that the place and size of the fluid connection influences the vibration behaviour. The connection part was not in the model but boundary conditions were chosen such that they represented the different fluid connections (see also Fig. 5.3. The rest of the device was divided up in sufficient elements to have satisfactory calculation accuracy with short enough simulation time.

Results

The results of a calculation run consist of a list of frequencies of resonance modes and the corresponding mode shapes. The higher the frequency, the more complex the modeshape. A series of modeshapes from a particular device can seen in table 5.4. Here the first 29 calculation results are shown, in theory this series continues until infinity.

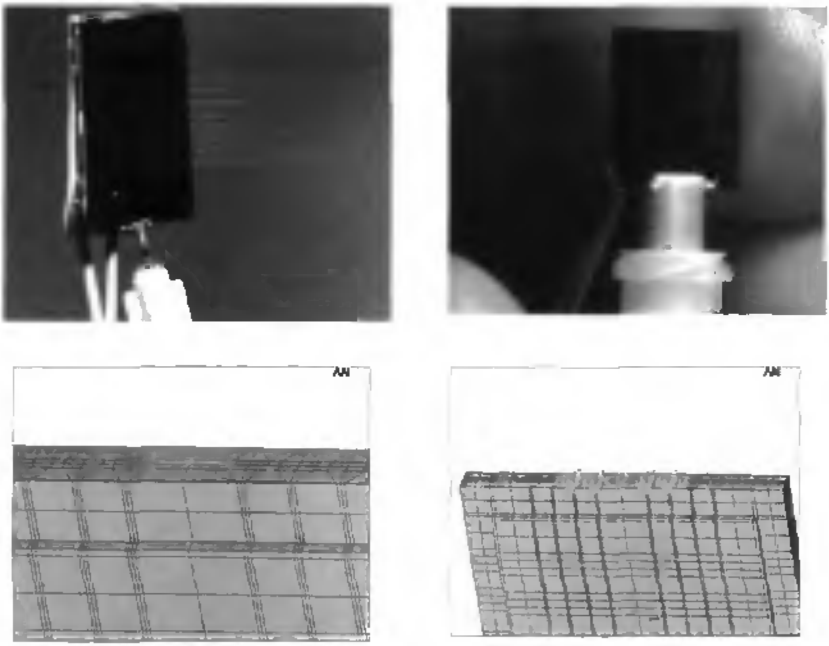

Figure 5.3: The different fluid connections and their FEM equivalent. The diamond symbols represent points in the models that are fixed in the three coordinate directions. For the needle only a small portion of the side is fixed while for the PEEK connection more of the side is fixed.

Figure 5.4: A series of modeshapes of a 10x10mm² device. The diamond symbols are again the points in the model that are fixed. The numbers under the pictures are the modeshape number and the frequency of the mode. Only the front side with the nozzles is shown. The backside can be seen moving through the frontside there where the movement of the backside is opposite that of the front side, for instance in modes no. 7, 11, 16 etc. The amplitudes are give as relative values, and normalised to 1. (next pages)

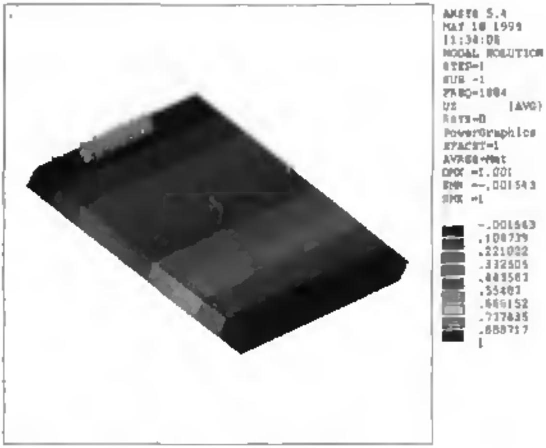

1; 1884 Hz

2; 12939 Hz

3; 23724 Hz

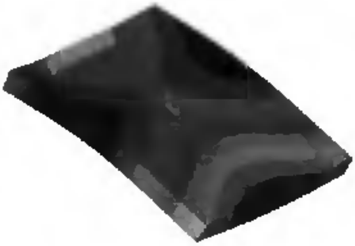

4; 35023 Hz

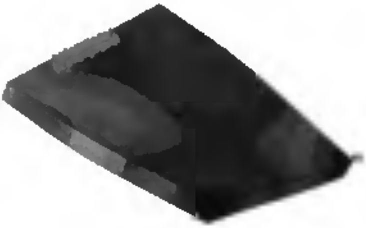

5; 48240 Hz

6; 48793 Hz

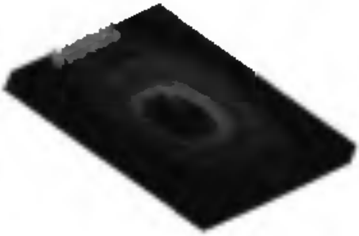

7; 56101 Hz

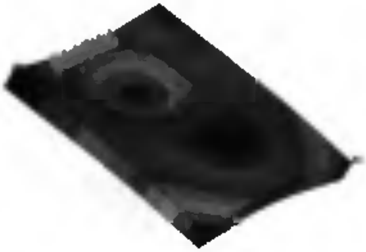

8; 69523 Hz

9; 73421 Hz

10; 81771 Hz

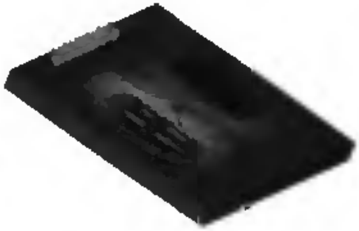

11; 89985 Hz

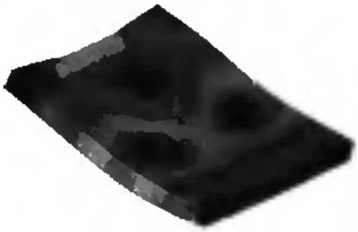

12; 100734 Hz

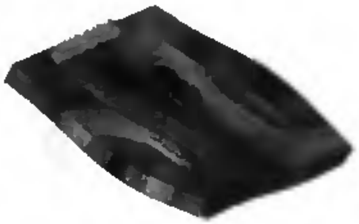

13; 107517 Hz

14; 113495 Hz

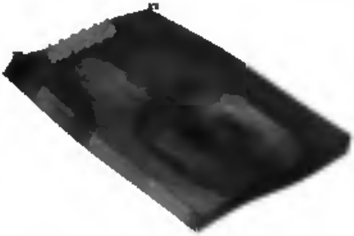

15; 114676 Hz

16; 126211 Hz

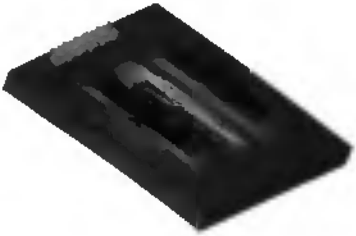

17; 135433 Hz

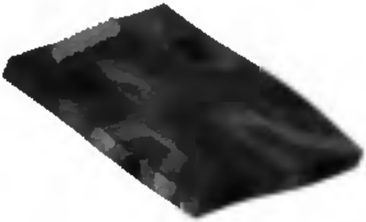

18; 140385 Hz

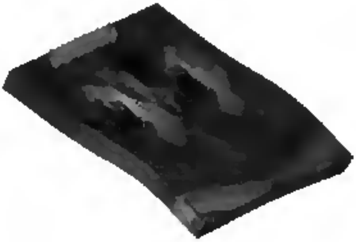

19; 142606 Hz

20; 146685 *Hz*

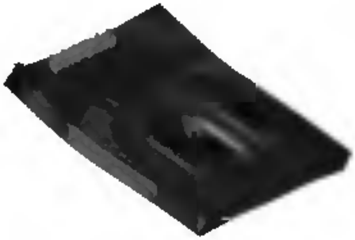

21; 151332 Hz

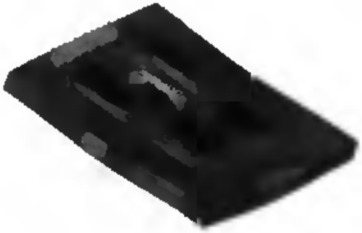

22; 159937 Hz

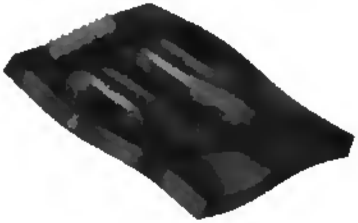

23; 160211 Hz

24; 171406 Hz

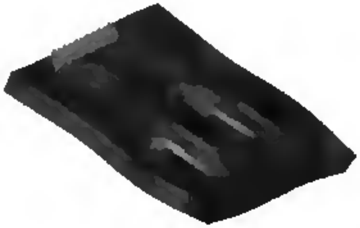

25; 171657 Hz

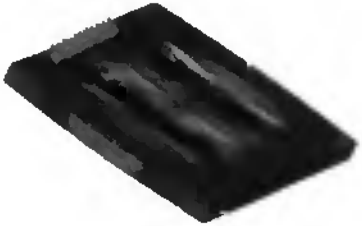

26; 180573 Hz

27; 184168 Hz

28; 185298 Hz

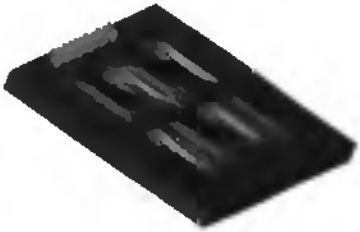

29; 195334 Hz

It is possible to name modes according to the number of extremes in both axes. For instance mode 7 can be called a 1,1 mode, while mode 8 is a 2,1 mode. There are several different kinds of modeshapes. The first ones (for instance modes 1 through 6) are body modes, the device vibrates in a similar fashion as a massive plate. Here the backside moves in the same direction as the front side, and with the same amplitude. No droplet ejection is possible with these modes. Modes 7 and 8 are the first ones where the front side moves differently from the back side. These modes could be used for droplet ejection. Mode 9 and 10 are again body modes, this time more complicated then the first ones. The series of body modes continues through the whole frequency range. Mode 11 is similar to mode 9, but now the back side moves in the opposite direction. Mode 16 is comparable with mode 11 only 90° rotated. This is due to the asymmetry introduced by the fluid connection. Without the asymmetry they would be at the same frequency. Modes 15 and 20 show another possible vaporising mode; the 2,2 mode.

As conclusion can be said that there are body modes that can not be used for ejecting droplets and there is a second series of modes that can be used for droplet ejection. As third, modes are found with a very complicated vibration behaviour which do not fit in any of the previous two descriptions, e.g. modes no. 13, 14, 18, 25, 26, 27 and 28.

5.3.2 Validation of the model

With so many assumptions in the model, empty fluid chamber, fluid connection through boundary conditions, but also the influence of the electrical connections and the stress due to the assembly procedure, it was important to validate the simulation system. To do this FEM models were made of several existing vaporisers. With the aid of these results it was possible to identify the modes of interest. This first simulations also helped minimize the calculation time to 45min. The main validation instrument was the interferometer, showing us the modeshapes on the front surface of the device. Fig. 5.5 shows two typical results of the comparisons,

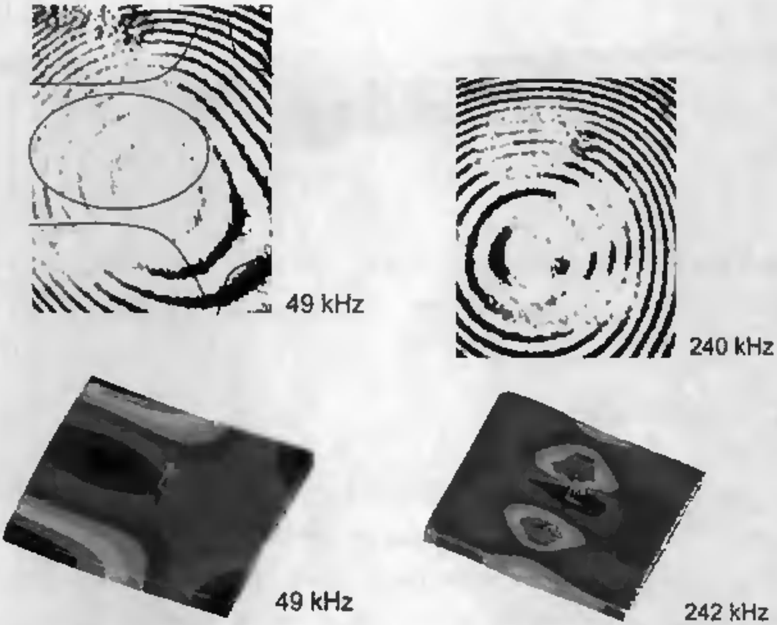

***Figure 5.5**: Two typical comparisons between a simulated mode and the measured vibration of the front side of the device*

both the simulation and interferogramme are from a device without water in the fluid chamber. The agreement is good. From the shown observations and numerous others the reliance interval for the simulations was set to 5%. It is important to notice that the order of the modes as they appear in the calculation and as they appear in the interferogrammes is the same. Already in chapter 4 the comparison between an empty and filled device was made. With this there is enough evidence to say that simulation of an empty device is sufficient for doing predictions on a filled device.

Figure 5.6: *Cut through the device clearly showing the effect of the optimisation criterium; same movement on the back and front side but in opposite direction.*

5.4 Optimisation

The simulation platform is now validated and can be used to find the optimum design. It was already seen that the backside (piezo side) of the device did not always have a compatible pattern with the front side. It is even possible that the back side movement completely cancels that of the front side (body modes). This gives the first optimisation criterium: the shape of the mode on the front and backside should be the same but in opposite direction (see also fig. 5.6). Connected with this comes the second criterium: the amplitude should be as high as possible over a maximum area.

It is not possible to optimise a device for all possible resonances because of the fundamental asymmetry between the front and backside, given by the piezo. So a certain 'target' mode was chosen for each of the optimised devices. From the validating simulation certain modes were seen to appear with a rather simple modeshape (low modeshape numbers) at frequencies that are interesting for droplet ejection. The earlier devices had problems with nozzles that started leaking due to insufficient amplitude that they received. Choosing one particular mode shape makes the placement of the nozzles easier, it is known where the maxima in amplitude will occur, minimizing the chance of leakage.

Due to a limited quality factor (due to damping) mode mixing was seen for modes that appear close to each other. This can be observed on the interferometer as a slowly changing pattern on the front plate when a frequency scan is made.

When there is no mode mixing one mode appears after the other with a certain area of 'no movement' in between. The larger the frequency distance between two modes the better this separation. (see also the discussion on the quality factor on page 63). When mode mixing occurs it is much harder to get the device to vibrate in one particular mode. This gives the third criterium as: the frequency distance between the mode of interest and the ones adjacent should be as large as possible.

To achieve all this, certain aspects of the geometry have to be changed. The thickness of the two silicon parts, the size of the funnels, the thickness of the membrane etc. A few restrictions were applied;

- The total size of the device was not changed as compared to the device proposed in chapter 3; Total wafer thickness stays 400 μm and the chip size remains 10 x 10 mm^2.
- The front side remains as much as it is because we need to put all the nozzles in the device and the device already functions reasonably well. Also the size of the nozzle membranes was kept constant to prevent them from being blown out by the pressure pulse.
- The fluid connection remains the same for convenience on system level.

This leaves the back membrane and the width of the connecting rim as free parameters for optimisation. Also the placement of the nozzle funnels is still free to choose.

After identifying three modes of interest, three different device designs were optimised each for one of these modes using the above three criteria. The three devices were named Vapo8, Vapo10 and Vapo11.

A very important step in the optimisation was to realise that the backside as it was would never achieve the right vibration behaviour at the right frequency. The front side is in fact a membrane with etched out cavities and thus has a lower effective mass but similar total stiffness. Formula 5.4 can be used to find an equivalent back membrane that has the same resonance frequency. By making the back membrane thicker it can also be made stiffer but the effective mass goes up as well, giving a unrealistic thickness to arrive at a similar resonance behaviour as the front

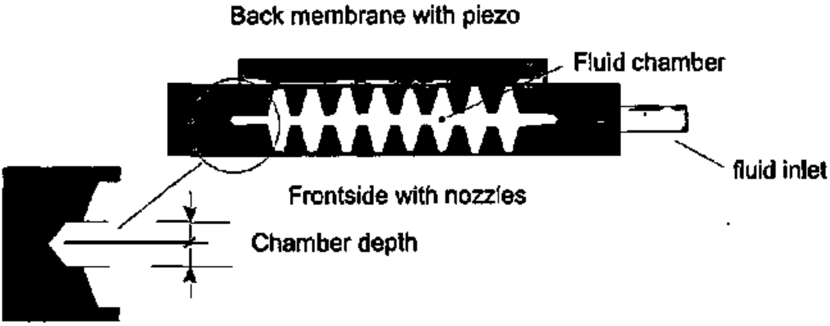

Figure 5.7: *The new device design with similar back and front side*

side. This would give problems in the amplitude. If now for the back side a similar type of membrane as for the front side is used this situation can be improved. Now only the piezo is left as asymmetry in the design. Fig. 5.7 shows this new design. Main parameter left for the optimisation is now the depth of the two chamber sides. Secondary the width of the rim and the size of the piezo are of importance as well as the size of the fluid connection. The cavities for the nozzle membranes are placed such that the they correspond to the maxima in the amplitude for the targeted mode. Fig. 5.8 shows schematic drawings of the basic layouts of the three new designs. The next paragraphs will go into details of the simulation results of each of the designs.

5.4.1 Vapo 8

This design addresses the (2,2) modes of the front and back side. This ideal mode is shown in fig. 5.9, it has two extremes on the two main axis. The basic layout is given in 5.8.

Fig. 5.10 shows the influence of the depth of the two chamber sides on the resonance frequency and the frequency distance. The designs coded Vapo8–50e and Vapo8–75a have the best score for the frequency distance in this series. The numbers indicate the depth of the fluid chamber, when two numbers are given the first one is concerned with the frontside chamber half, the second one with

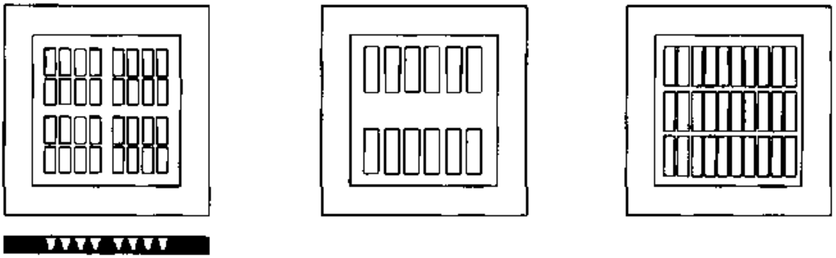

Figure 5.8: *Layout of the new designs, each device consists of two similar silicon parts with a piezo on one side (see also fig. 5.7). The left layout is for Vapo 8, targeted for the 2,2 mode. Cavities are place there where maximum amplitude is expected. The middle one for Vapo 10, targeted for the 2,1 mode at a lower frequency then vapo8. Also here the nozzle cavities where maximum amplitude can be expected. The right most design of Vapo 11, a higher frequency then Vapo 8 with a 3,1 modeshape.*

the backside. Letters indicate different boundary condition (e.g. different fluid connections).

The influence of fixing a point on the boundary can be seen from fig. 5.11. Also in this figure the influence of the size of the piezo actuator. It can be seen that fixing a point has positive effect for the frequency distance criterium. The influence of the size of the piezo is marginal. For several devices the amplitude criterium was also tested, results can be seen from fig. 5.12. The third design clearly has the higher amplitude. Final design as it is made is comparable with the vapo8-75a from fig. 5.11 and has a theoretical resonance frequency for the 2,2 mode of 216.5kHz.

Finally a comparison was made with the actual device. Fig. 5.13 shows the interferogrammes from two different devices vibrating in the target mode. As was expected the two devices show the targeted mode at the predicted frequency.

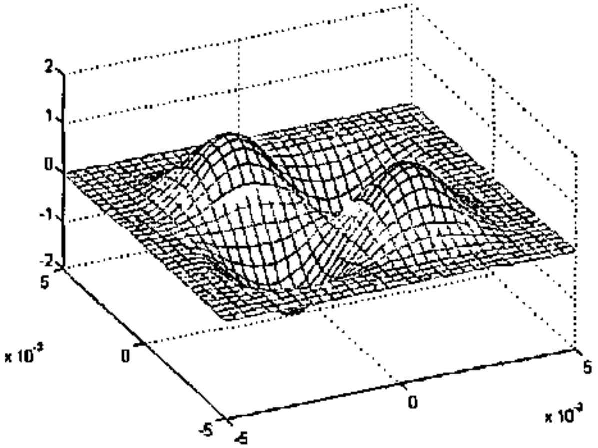

***Figure 5.9**: The 2,2 mode*

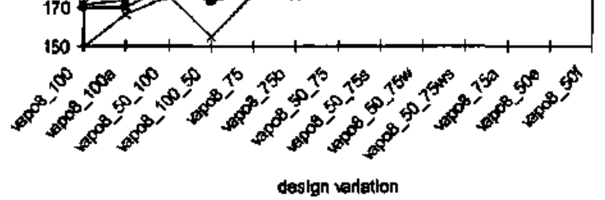

***Figure 5.10**: Resonance frequency of the 2,2 mode and the neighbouring modes for variations of the design Vapo8. The different designs have different depths of the two sides of the chamber (see text).*

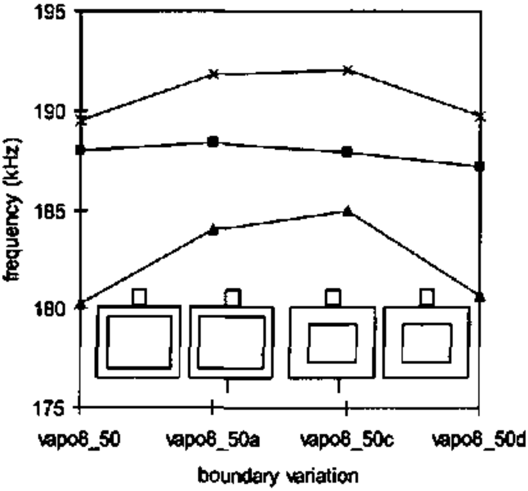

Figure 5.11: The influence of the boundary conditions and the piezo size on the frequency distance. As in fig. 5.10, the middle curve is the target mode. The line represents a fixed point on the device. The influence of the piezo size is marginal. Fixing an extra point on the side has positive effect in these cases.

5.4.2 Vapo 10

For the design of vapo10 the (2,1) mode is addressed. There exist two possibilities for this mode; the (2,1) or, as seen in the same direction, (1,2). Theoretically they appear at the same frequency for a rotational symmetric device. The fluid connection will cause an anti-symmetry in the device and thus a frequency distance between the two possibilities. The basic layout of this mode is also given in fig. 5.8.

The influence of the connection to the outside world can be seen from fig. 5.14. The best result, i.e. the best distance for the two adjacent modes, was achieved with only a point connected. This is less practical and the difference with devices with a small portion of the side connected is marginal (design nr 3 from fig. 5.14). These result was used further to maximise the amplitude of the (2,1) mode on both sides to arrive at Vapo10-X, which has the targeted mode at 126.2 kHz.

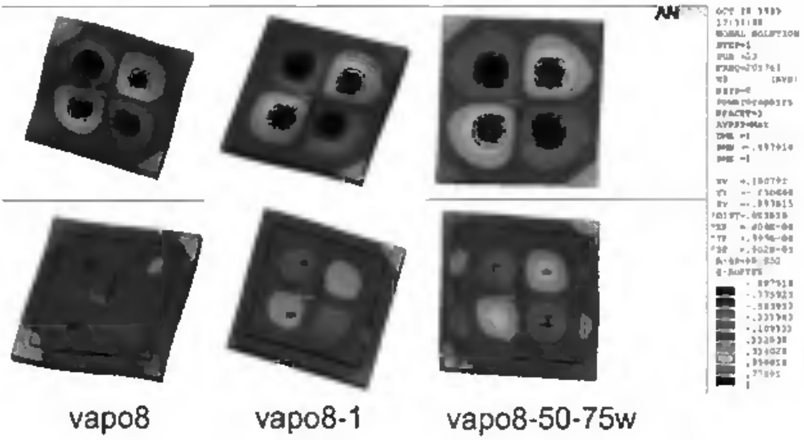

Figure 5.12: *Amplitude of the 2,2 mode for different versions of Vapo8. The top shows the front of the device and the bottom the backside (with the piezo). The third design has a wider connection rim and shows a higher amplitude on the backside.*

5.4.3 Vapo 11

This design addresses the (3,1) mode which has fundamentally a higher frequency than the two previous designs. The advantage of the higher frequency is the lower number of nozzles necessary to arrive at the same flow.

This design proved very sensitive to boundary conditions and also to slight variations in the design. This already indicated that slight variations in the production and assembly would perturb the functioning of the device and this was confirmed by experiments.

Fig. 5.15 shows three calculation results for one geometrical variation of vapo11 with three different sets of boundary conditions. In the first case the device was only connected at the place where the fluid connection sits (similar to the syringe needle). The second case has an extra constraint at the opposite site and the third has also constraints there where the two nodal lines meet the right and left side of the device. It can be seen that especially the backside is enormously influenced

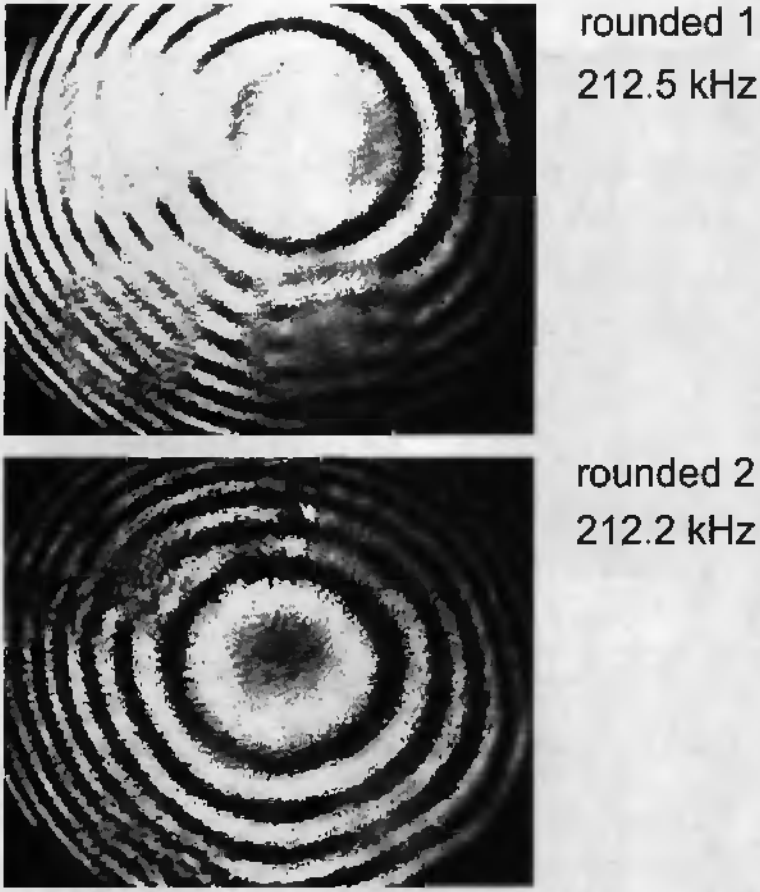

***Figure 5.13**: Interferogrammes of two different Vapo8 devices. The top picture is taken at 212.5kHz and the bottom one at 212.2kHz.*

by these changing boundary conditions. What is also remarkable is that the targeted mode changes mode number between cases two and three, which means that certain modes disappeared.

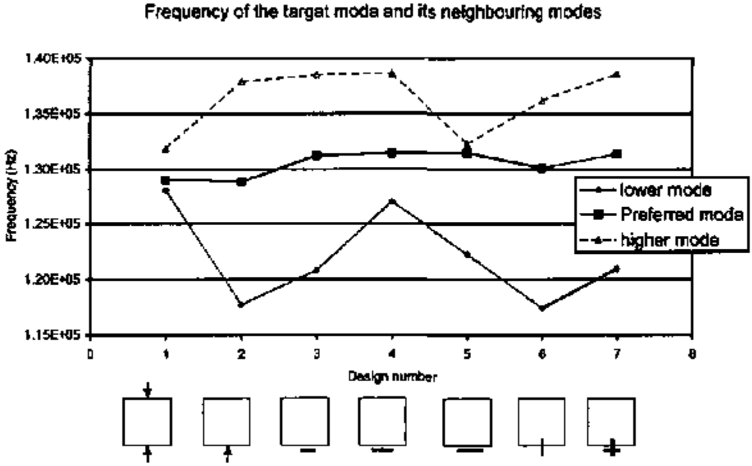

Figure 5.14: Influence of the fluid connection on the frequency distance criterion for the Vapo10 design. Arrows indicate a fixed point. The lines represent area's that are fixed. Designs 6 and 7 perform the best, but also 2 and 3 are acceptable. These designs will be submitted to the other criteria.

5.5 Conclusion and Discussion

For every device design, around 50 simulation runs were made, each for a different combination of the optimisation parameters. All results were 'manually' judged and in this way the ideal design was found. It is possible to fully automate the optimisation procedure.

Three designs were optimised using the three criteria:

- Movement of the backside similar to the front side but in opposite direction for maximum surface available for nozzles.
- Maximum amplitude between the front and backside, for maximum ejection pressure pulse.
- Maximum frequency distance between the target mode and its neighbouring modes for stability.

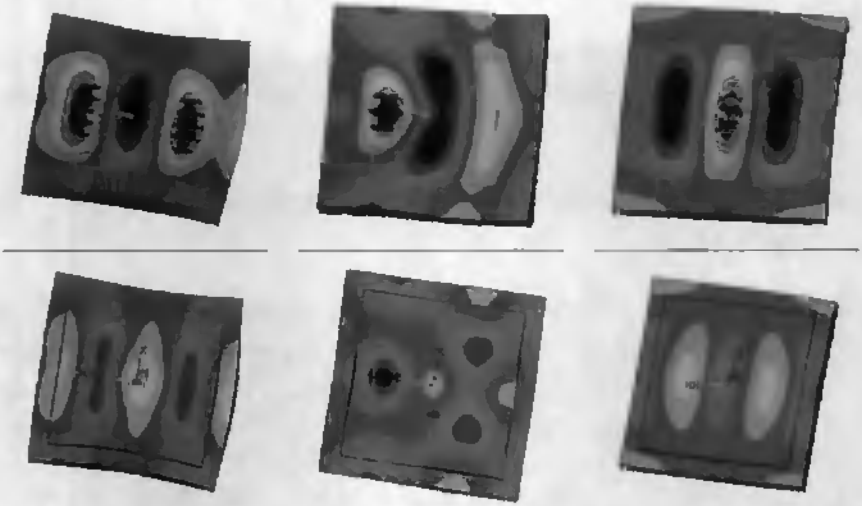

left: 28; 215.1 kHz middle: 28; 219.65 kHz right: 26; 219.4 kHz

Figure 5.15: *Three different boundary condition cases of a vapo11 version. Left; only the fluid entry connected, Middle; Also the opposite side of the fluid entry connected. Right: Added constraints there where the nodal lines cross the left and right side.*

These designs were fabricated and results were compared with the simulation predictions. The agreement is very good and more results will be presented in the next chapter. The modeshapes appeared at the predicted frequencies as could be seen with the interferometer and the impedance measurements. The design vapo11 proved too sensitive to slight variations so it is left out for the rest of the discussion.

Next step is to check whether the vaporisation characteristics of the designs vapo8 and vapo10, have improved compared with the ones available before the optimisation procedure. The next chapter will present the comparison of the characterisation results and the simulation predictions. Measurements on droplet size and throughput will also be presented.

Through the modelling and optimisation the fundamental understanding of the functioning of the device improved. It proved sufficient to model the empty device, to predict the behaviour of the filled device.

Bibliography

[5.1] E. Zauderer. *Partial differential equations of applied mathematics*. Wiley, New York, 1989.

[5.2] G.B. Warburton. The vibration of rectangular plates. *Proc. Instr. Mech. Eng. Ser.A*, 168:371–384, 1954.

[5.3] J-F. Manceau, L. Robert, F.O. Bastien, C. Oytana, and S. Biwersi. Measurement of residual stresses in a plate using a vibrational technique—application to electrolytic nickel coatings. *Journal of microelectromechanical systems*, 5(4):243–249, 1996.

[5.4] O.C. Zienkiewicz. *The Finite Element Method*. Mc. Graw–Hill London, third edition.

[5.5] *Ansys User's Manual for Revision 5.0*, volume IV, Theory. Swanson analysis systems Inc., 1992.

Chapter 6

The optimised device

6.1 Introduction

Three different, optimised designs were shown in the previous chapter. The simulation results were briefly compared with the fabricated devices, and two of the designs showed the predicted behaviour. The third showed unacceptable instabilities as could already be explained by the simulation results. These first two designs, Vapo8 and Vapo10, will be further tested. A thorough comparison will be made between the simulation results, the interferometer observations and the impedance measurement to conclude on the quality of the simulation results. Secondly these devices will be used as vaporiser and results compared with the demands set out in chapter 2.

For convenience, the numbers used in the simulations are dropped. Vapo8, resp. Vapo10, as it is presented in this chapter is the optimal design found in chapter 5 (Vapo8-75a, Vapo10-X).

6.2 Comparison of simulation results

To come to a full comparison, interferogrammes of several modes should be compared with the simulations. The impedance curves can be used as complementary information and can give information about the quality factor of the various modes.

With this final comparison the simulation platform will be further validated. Also can this information be used for extension of the simulation effort, for finding the amplitude of the calculated modes through dynamic simulation.

6.2.1 Vapo8

Some of the results were already shown in the previous chapter, for instance Fig. 4.7 on page 73 shows the comparison of the impedance curve of Vapo8 with the interferogrammes of the resonances. In Fig. 6.1 and 6.2 a different series of measurement results is shown for the same device. It can be seen that not only the targeted mode, the 2,2 mode, appears where it is expected but also the other modes show good agreement. Some of the theoretical modes could not be seen due to insufficient amplitude or due to mode mixing. Other modes were hard to find back in the impedance curve even though they showed up clearly in the interferometer.

The good agreement between the impedance curve and the interferogrammes is logic, they are made from exactly the same device. The simulation results show minor differences with the measurement results. A number of effects can cause this deviation.

- Numerical effects; The resonance frequencies are approximated during the calculations. The uncertainty, taken from the manuals of the simulation programme, is usually of the order of 1% or more.
- Discretisation errors: The FE-mesh is an approximation of the real problem. The fewer elements, the less accurate the calculation result. This error can account for several 0.1% of the error.
- Geometry differences: The fabricated device never has exactly the same dimensions as the simulation model. This can account for several percent of deviation.
- Damping: The calculation was done on ideal devices without damping. In reality the damping will cause the resonance to appear at a lower frequency. The amount of damping depends on the actual modeshape and can also cause up to several percent of deviation.

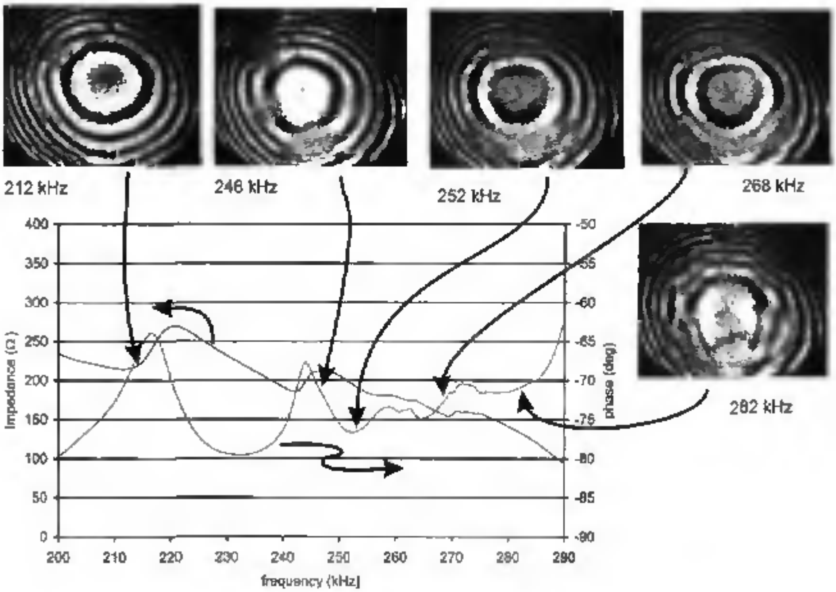

Figure 6.1: The interferogrammes and impedance curve for a Vapo8. Resonances correspond to bending points in the phase curve. The fluid connection is located on the top of the interferogrammes. Fig. 6.2 shows the corresponding simulation results.

The calculation results show good agreement with the fabricated devices, in view of these possible errors. The numerical and discretisation errors can be minimized by finer meshing and better calculation methods. This in turn will give higher demands on computer resources; e.g. memory and CPU speed.

6.2.2 Vapo10

Also for the vapo10 design the full comparison between the simulation results, the interferometer observations and the impedance curve was made. Fig. 6.4 and 6.3 shows this complete analysis. Again, the simulated modes could be found back within a few percent of the predicted frequency. Some of the resonances that clearly show up on the interferometer are hardly visible in the impedance

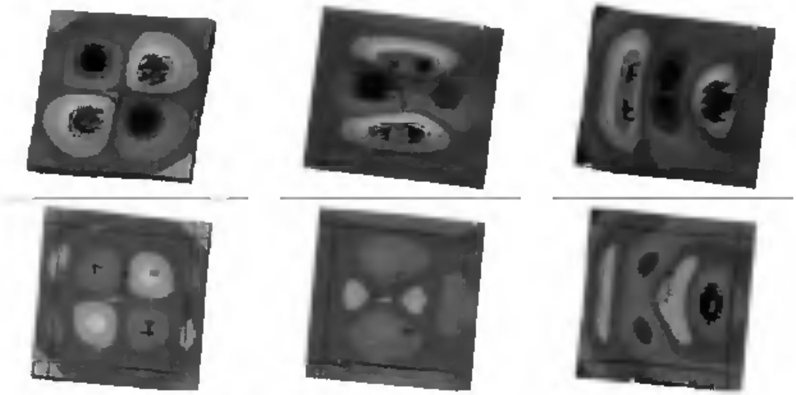

23: 201.35 kHz 25:234.6 kHz 28: 254.2 kHz

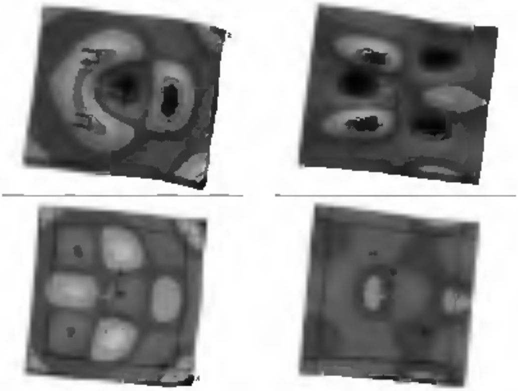

31: 271.1 kHz 33: 293.8 kHz

***Figure 6.2**: The simulation results for Vapo8 as it was fabricated. The fluid connection is on the left side of the device. These figures should be compared with the interferogrammes of fig. 6.1.*

measurement. Even the target mode at 126kHz (119kHz in the interferometer) has a very small phase change. This shows that the impedance measurement is not conclusive, but should be used in combination with the interferometer.

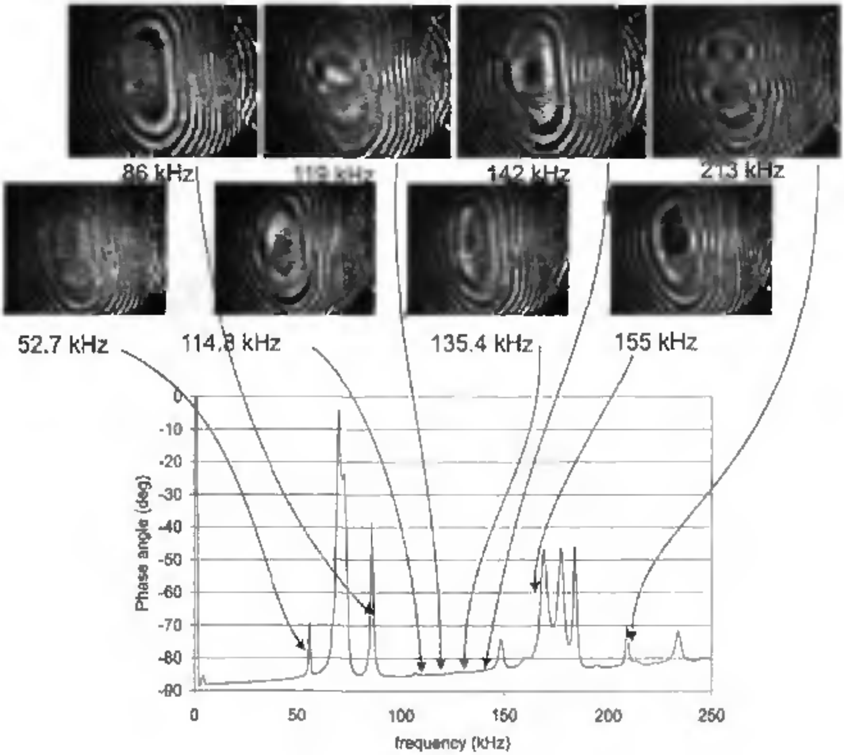

Figure 6.3: *The interferogrammes and phase angle curve for Vapo10.*

6.2.3 Stability

The stability of the target mode of Vapo8 in the frequency domain, which is connected with the mode mixing and the quality factor can be seen from Fig. 6.5. The mode distorts fast at frequencies beside the resonance frequency. This indicates a high quality factor.

The target mode moved about 3 kHz in frequency when the fluid chamber was filled with liquid. Important to notice is that there is a continuous transition, e.g, the target mode can be found somewhere between the empty and filled frequencies, when the chamber is not completely filled. Building a resonance circuit could

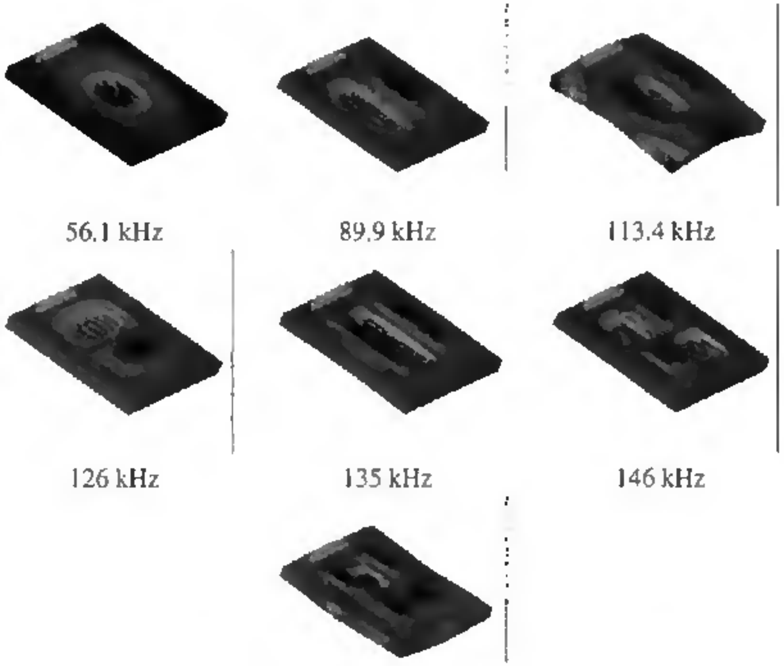

56.1 kHz

89.9 kHz

113.4 kHz

126 kHz

135 kHz

146 kHz

159 kHz

Figure 6.4: The simulation results for Vapo10

compensate the shift in resonance frequency to compensate for any air bubbles that might form in the fluid chamber.

6.3 Vaporiser characteristics of the optimised devices

6.3.1 Droplet size

The fabricated devices had nozzles of 8 μm diameter in stead of the demanded 5 μm, due to some fabrication problems. It is expected that the droplets have the same size, i.e. 8 μm. Fig. 6.6 shows a high-speed video picture of droplets generated from a Vapo8 with 8 μm nozzle size. The distance between two lines on the ruler is 50 μm. This gives for this small sample that the droplets are between

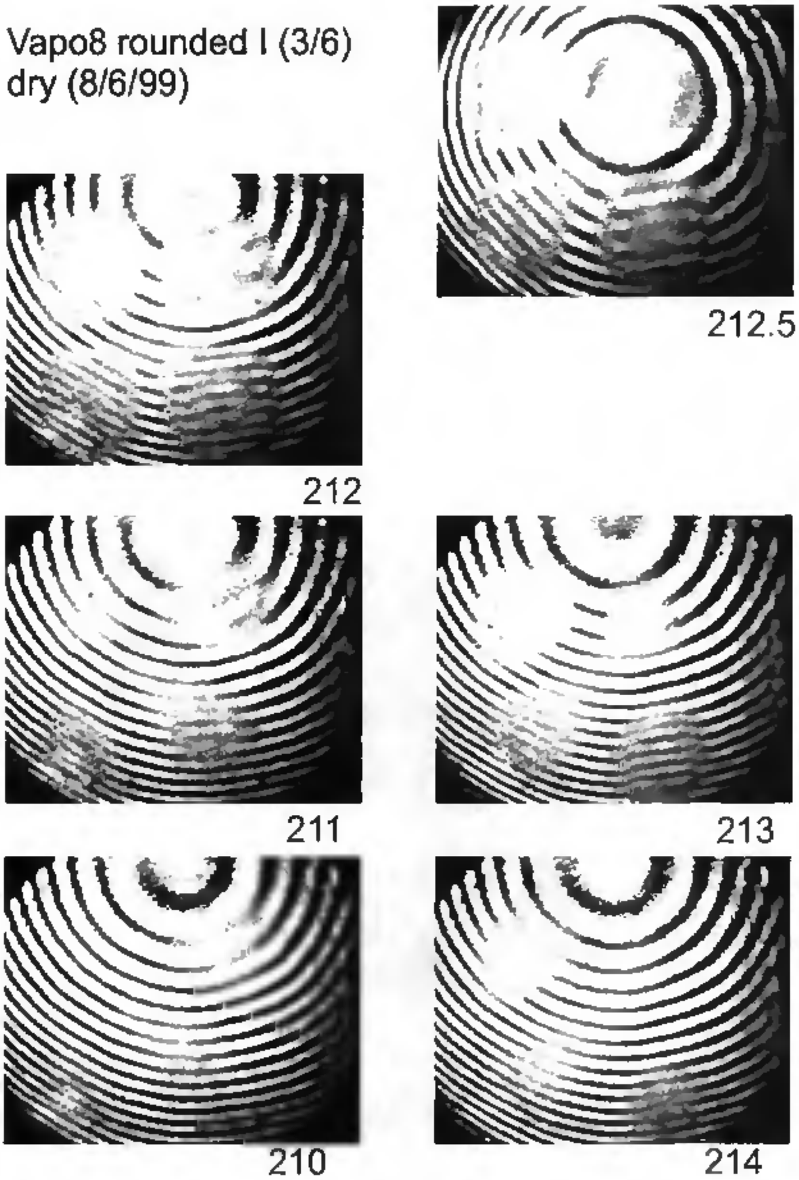

Figure 6.5: *Interferogrammes around the targeted 2,2 mode at 212.5 kHz. The numbers correspond to the actuation frequency in kHz.*

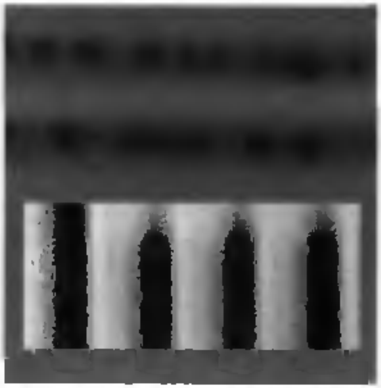

Figure 6.6: *High speed video picture of the droplets ejected from a Vapo8 with 8 μm nozzle size. Average droplet size is 8 μm.*

Figure 6.7: Overview of the nozzles in a Vapo8, nozzles were measured to be 8 μm in diameter.

7 and 9 μm in diameter. This confirms that the droplet diameter is given by the nozzle size. The actual nozzles are shown in Fig. 6.7. Unfortunately it was not possible yet to perform LDA measurements on these samples.

6.3.2 Throughput

The total flow and the flow stability are of interest for the final application. Measurements with the scale set-up (details in chapter 4), showed that there are stability problems. The shot to shot volume can vary as much as 25%. This is probably due to air bubbles that form inside the fluid chamber. The device was actuated with a $30V_{pp}$ sine signal and had a power consumption of 1W.

These air bubbles are drawn in from the outside through the nozzles. The depression in the fluid chamber due to the flow through the chamber in combination with nozzles that do not see sufficient amplitude can explain this. Cavitation seems out of the question due to low accelerations in the device. Degassing of the liquid in the fluid chamber can also be a problem, but tests showed only minor influences when using degassed water. Air in the fluid chamber changes the vibration behaviour and thus the mode shape. This in turn modifies the available pressure pulse at the nozzles.

Fig. 6.8 shows again (also fig. 4.17) the measurement results for different frequencies around the targeted resonance. The instability is clear from the spread in measurement data. At frequencies besides the measured range the flow tended very fast to zero. When only the maxima are taken the impedance curve can be found back in the flow, confirming the assumption that the ejection is resonance dependent. The small spread at 207.0 kHz can not easily be explained nor reproduced, but is possibly connected with a larger air bubble that stabilised the system at a lower flow. The stability is still insufficient to de repeatable the measurements.

When there are no air bubbles present in the fluid chamber the device works with a maximum efficiency and will give the maximum flow possible. The measured peak flow was $20\,{}^{\mu L}/_{s}$ (data not shown in fig. 6.8). Considering that droplets of 8 μm diameter hold four times more volume than the target of 5 μm, the total flow can be estimated to be 5 ${}^{\mu L}/_{s}$ for the target size range. This is slightly lower than the demand of 10 to 15 ${}^{\mu L}/_{s}$. Improving the stability by preventing air bubbles from forming will improve the total flow to within the proper range.

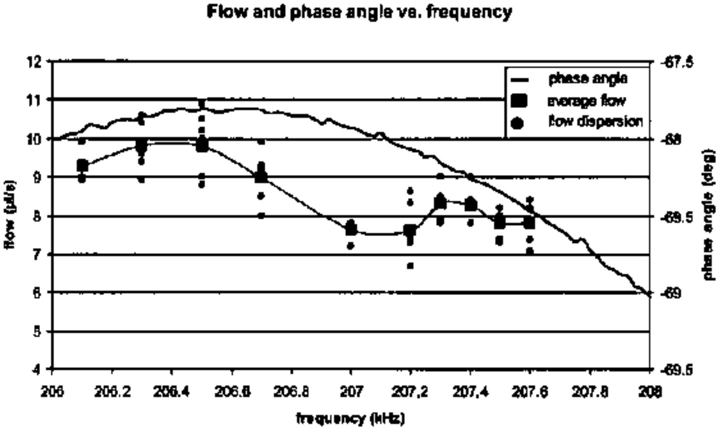

***Figure 6.8**: Typical flow measurement using the scale (repeated from chapter 4), compared with the phase angle of the impedance measurement. Data points are results of a single measurement.*

With the instabilities caused by the air bubbles the device still showed some of the leakage from nozzles that do not receive sufficient amplitude. By treating the front side of the device with HMDS,[1] which makes it hydrophobic, leakage could be minimized or even prevented. This is a large improvement compared with the previous designs. HMDS is not useful for medicine applications because of its toxicity but other coatings can be found that have the same properties.

Although not characterised in detail, the device seems to be sensitive to the impedance of the fluid reservoir and the connecting tubing. Different kinds of connections gave different stability behaviour. This should be investigated in subsequent research.

Two optimised designs are presented in this chapter. Both of them showed some problems with air bubbles. They both showed far better characteristics concerning the leakage. Vapo 10 works at a frequency of 120kHz while vapo 8 works around 210 kHz, this gives Vapo 8 a flow advantage. Also has Vapo 8 a clearer

---

[1] HMDS = hexamethyldisilazane

peak in the impedance/phase diagramm which makes it easier to design electronics for the resonance circuit. Vapo 10 works at a lower frequency and has therefor a higher amplitude with the same actuation signal, this would lower the power demand.

Concluding can be said that there is at this point no clear advantage of one design over the other. Further testing, especially the droplet diameter, is necessary to come to a conclusion.

6.4 Further work

A small phase change at the targeted mode means that it will be difficult, but not impossible, to design electronics that could compensate for any shifts in resonance frequency. Further research is necessary here.

An other solution to the same problem could be to look at other target modes that maybe have a larger phase change. The advantage of using a mode that has a phase change close to 90° is the low ohmic power consumption.

Properly designed electronics can also compensate for the differences between the different vaporisers; not all devices will have exactly the same resonance frequency due to small production and assembly variations.

The total flow is not stable enough for the application, this seems connected with the forming of air bubbles inside the fluid chamber. The fluid capacity at the entrance and the connection to the fluid reservoir, seems to influence this problem. Fully analysing this behaviour will show how to stabilise the total flow.

The hydrophobic coating on the outside improved the remaining leakage behaviour. The influence of hydrophilic coating on the inside still has to be further investigated.

Now that the basic operational parameters of the device are understood and a simulation platform is available, it will be possible to do rapid prototyping with different materials for certain parts of the device. Especially the backside has not necessarily to be made in silicon technology. Injection moulding of ceramic seems a good option, it is much cheaper in mass production and ceramic has mechanical properties that are compatible with the silicon of the front side. For the frontside with the nozzles, there does not seem to be an alternative that can achieve the same fabrication accuracy.

6.5 Discussion and Conclusion

Starting form a basic understanding of the vaporisers as presented in chapter3 a modelling and optimisation effort was started. Three optimised designs were fabricated and in this chapter two of the optimised designs were fully tested and compared with the predictions of the previous chapter. The agreement is very good. This means that the basic operational parameters of the device are understood and modelled correctly.

The simulation proved very useful for the improvement of the vaporiser. The leakage could be prevented and the stability problems could be minimized to these caused by the air bubbles in the device. Also are the operational parameters better understood so that the remaining problems can be easily identified. A design was fabricated that functioned with a certain mode, making it possible for the first time to place nozzles in area's with maximum amplitude.

The size of the droplets can be changed at will, by etching the desired nozzle sizes. The target size of 4 to 5 μm was already demonstrated in chapter 4. In this chapter it was seen again that the droplet size is give by the size of the ejection nozzle. Only a small spread in droplet size could be seen, probably due to the difference in actuation amplitude at the different nozzles.

The total flow is slightly too low and has some stability problems, but is in the right order of magnitude. This shows that the proposed design is suitable for the application.

The available designs before the optimisation procedure was started showed many problems due to leakage of nozzles that did not receive sufficient amplitude for droplets to be ejected. The improved designs, vapo8 and vapo10, did not show this problem because the nozzles are placed there where maximum amplitude is expected.

The power consumption of 1W for the device is reasonable; battery operation, and thus a portable device, will be possible.

Finally can be said the ink-jet techniques proved very successful. The spread in droplet size is far less as compared with the traditional devices. The proposed drop on demand devices are active elements which gives the possibility to build a 'smart' inhaler, which adapts its flow of medicine to the inhalation flow of the patient.

Chapter A

Publications

The work presented in this thesis is also published in the following ways:

A.1 Patents

- 97120287.4-2305 Liquid droplet spray device for respirator therapies. Inventors: J. Hess, Hu Bo, R. Weber, I. Ortega, C. Barraud, B. van der Schoot, N. de Rooij, B. de Heij.
- 98111497.8-2305 Liquid droplet spray device for an inhaler suitable for respiratory therapies. Inventors: J. Hess, Hu Bo, R. Weber, I. Ortega, C. Barraud, B. van der Schoot, N. de Rooij, B. de Heij.
- 98122751.5-2307 Optimised liquid droplet spray device for an inhaler suitable for respiratory therapies. Inventors: J. Hess, Hu Bo, R. Weber, I. Ortega, C. Barraud, N. de Rooij, B. de Heij.
- 99122535.0-2311 Optimised liquid droplet spray device suitable for an inhaler for respiratory therapies. Inventors: J. Hess, Hu Bo, R. Weber, I. Ortega, C. Barraud, N. de Rooij, B. de Heij.

A.2 Conference and workshop presentations

The work in this thesis was presented, in parts, at the following conferences and workshops:

- Nanotech'97, Nov. 1999. Montreux, Switzerland. A device for dosing in the fL range, B. de Heij, B. van der Schoot and N.F. de Rooij.
- The first Swiss-Rumanian workshop on microfluidics. Lausanne, Switzerland. A device for dosing in the fL range, B. de Heij, B. van der Schoot and N.F. de Rooij. and A smart inhaler,B. de Heij, B. van der Schoot, Hu Bo, J. Hess and N.F. de Rooij.
- MSM'99, May 1999. San Juan, Puerto Rico. Modelling and optimisation of a vaporiser for inhalation drug therapy. B. de Heij, B. van der Schoot, Hu Bo, J. Hess, N.F. de Rooij.
- Eurosensor XIII. Sep. 1999. Den Haag, the Netherlands. Characterisation of a fL droplet generator for inhalation drug therapy, B. de Heij, B. van der Schoot, Hu Bo, J. Hess, N.F. de Rooij.
- The First, Second, Third and Final Minast convention. Bern, Switzerland. Intelligent microfuidic systems, proj. no. 1.06.02.

A.3 Conference proceedings

- Modelling and optimisation of a vaporiser for inhalation drug therapy. B. de Heij, B. van der Schoot, Hu Bo, J. Hess, N.F. de Rooij. Proceedings of MSM'99, San Juan, Puerto Rico. pages 542–546.
- Characterisation of a fL droplet generator for inhalation drug therapy, B. de Heij, B. van der Schoot, Hu Bo, J. Hess, N.F. de Rooij. Proceedings of Eurosensor XIII, Den Haag, the Netherlands. pages

A.4 Journal Publications

Characterisation of a fL droplet generator for inhalation drug therapy. Sensors and Actuators, B. de Heij, B. van der Schoot, Hu Bo, J. Hess, N.F. de Rooij. Accepted for publication in Sensors and Actuators A, the Eurosensor XIII special issue.